Master of Science in Physics
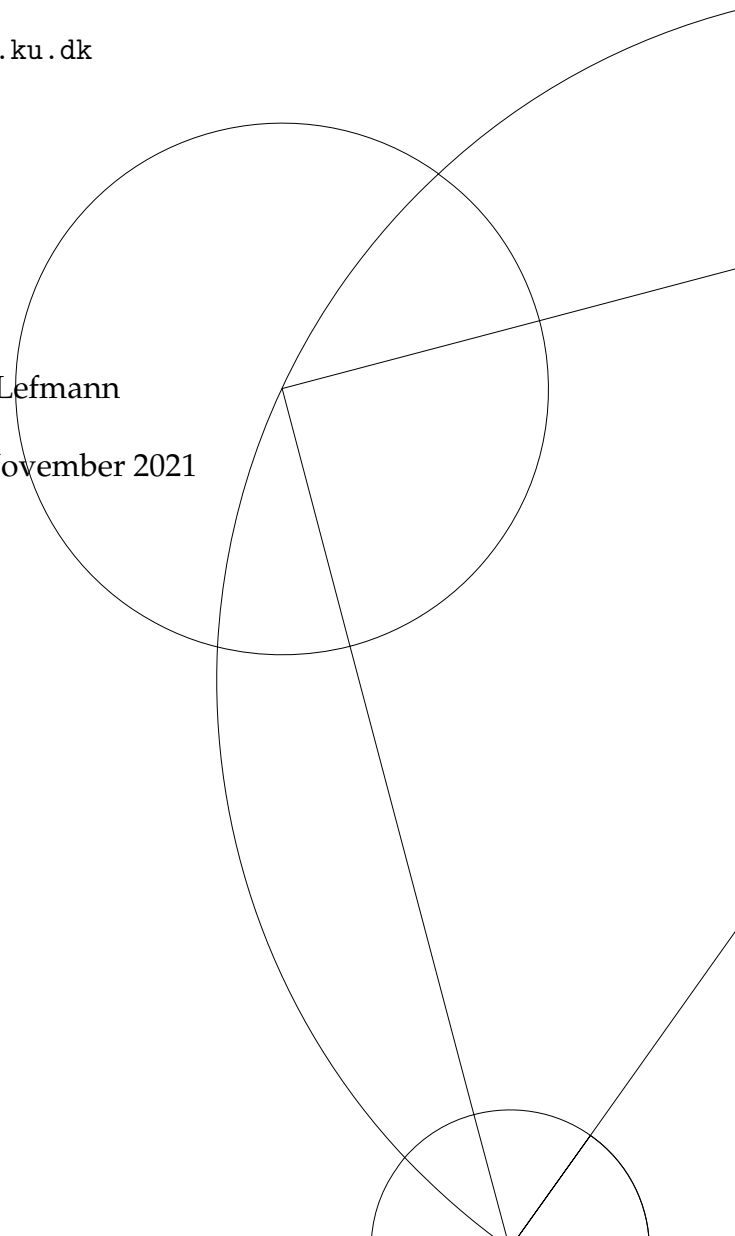
RLexact simulations of Azurite

Kris Marco Hoffmann

zql906@alumni.ku.dk

Supervisor: Kim Lefmann

Submission date: 15 November 2021

Abstract

Azurite is a mineral found in nature. It has some fascinating properties such as the fact that it is a 1D diamond chain with $S = \frac{1}{2}$ and antiferromagnetic exchange constants, which makes azurite a frustrated magnet. The frustration in azurite gives a $\frac{1}{3}$ magnetization plateau. This has gained a lot of interest from researchers in condensed matter physics. Since there is lacking a model that fully describes azurite I will in this thesis perform numerical many-body calculations with exact diagonalization to look at the excitation spectrum and the magnetization curve to describe the different models used in recent research.

Contents

Acknowledgements

1 Introduction

Blue pigment was used to paint Egyptian hieroglyphs, dye cloths and used in japanese paintings [18]. The blue pigment was a natural mineral called azurite ($Cu_3(Co_3)_2(OH)_2$). As said it has been used in paintings since it has a beautiful intense blue color, which is caused by the crystal field splitting of Cu 3d orbitals in square planar coordination.

In recent years azurite has come into the researchers scope due to a discovery of a plateau at $\frac{1}{3}$ of the magnetization of the material. This has made this material quite interesting and researchers are trying to figure out why this is the case. For this research many models have been tried, and in the most resent research the distorted diamond chain has been in use, but there is still discussion going since this model does not describe the properties of azurite fully.

To understand what models have been used I will in this thesis go through some of the most recent studies of azurite to try to clarify which model describes which properties of azurite well. To do so will I look at the most used model, which is the diamond chain model. In which all of the spins of Cu^{2+} are $S = \frac{1}{2}$. This model with the different exchange constants from the different articles, I will use to try recreating the data from experiments and calculations done on azurite. This will be done by exact diagonalization with the program RLexact.

This thesis will concentrate on the $\frac{1}{3}$ magnetization plateau and the excitation spectrum of azurite calculated by RLexact to get a better understanding of which models describe which property of azurite the most accurately. From this, the conclusion is that RLexact is able to use the model for the 1D diamond chain to describe the magnetization curve and excitation spectrum.

2 Quantum magnetism

Magnetic materials have been a part of the condensed matter physic studies for quite some time, but it is still a big and active field. This chapter is to give the most essential knowledge about the topics needed for my thesis, including exchange interaction and frustration [5][1].

In condensed matter magnets are typically put into two groups, ferromagnets and anti-ferromagnet. A ferromagnets has all spins pointing the same direction. Antiferromagnets (as a classical Ising with spin pointing up and down) the spins will anti-align so when there is a spin pointing up its neighbors will point down. This is more complicated when seen from a quantum magnetic viewpoint.

2.1 Quantum Magnetism Basics

To take a classical approach I will start from electromagnetism. From here we know that if there is electricity running through a loop there will be induced a magnetic field. If this concept was downscaled to the atom level and took a look at the electrons, it is possible to think the spins to be a small loop with a charge, which induce a magnetic field. This is called a magnetic moment ($d\mu$). The equivalent interaction between two spins creates a magnetic dipole moment. The total magnetic moment (μ) for a material is all the small moments ($d\mu$) summed up.

$$\mu = \int d\mu \tag{1}$$

In atoms the magnetic moment is explained by the electrons orbiting around the nucleus in the same direction as the angular momentum (**L**) of the electron. In this case the magnetic moment will be written as:

$$^- = \gamma \mathbf{L} \tag{2}$$

If we take a quantum mechanical view of the system, we have the orbiting electrons with the angular momentum **L**, and the intrinsic spin angular momentum **S**. These are coupling together and therefore **L** and **S** are not good quantum numbers. To get a good quantum number we introduce the total angular momentum as

$$\mathbf{J} = \mathbf{L} + \mathbf{S} \tag{3}$$

2

Since this thesis is going to concentrate around Cu^{+2}, which is a $3d^9$ ion and therefore the orbital moment will be quenched due to the crystal field, meaning $\mathbf{L} = 0$.

For magnetic materials is more interesting to know how many magnetic moments there are per unit volume to be able to compare magnetic materials, since there are to many atoms in a material and therefor to many to count and this will grow as the material. Magnetic moments per unit volume is the definition of the magnetization ($\mathbf{M}$) that can be considered to be a smooth vector field, continuous everywhere on the magnetic material except the edges.

2.2 Exchange Interaction

To be able to talk about the exchange interaction we need to start with the magnetic interaction, which can be thought of as two magnetic dipoles in vacuum. These two dipoles μ_1, μ_2 has a distance between them of $\mathbf{r}$, the interaction between these two dipoles has the energy of:

$$E = \frac{\mu_0}{4\pi r^3} \left[\mu_1 \cdot \mu_2 - \frac{3}{r^2} (\mu_1 \cdot \mathbf{r})(\mu_2 \cdot \mathbf{r}) \right] \tag{4}$$

as seen the energy is dependent on the separation and the alignment of dipoles. The main free parameter is the distance between the dipoles, which makes the energy decrease rapidly the further the dipoles are from each other. If we take two electrons and say the distance between them is 1 Å the energy of the exchange will be as small as $10^{-23} J = 1K$, which is a really weak interaction, since most of the magnetic ordering happens at higher temperatures, and therefore will in most cases not be used.

As said before one of the strongest interactions to gain magnetic order, one of the strongest interactions is the exchange interaction and it is therefore the primary mechanism. Since electrons are in the main seat of the exchange interaction, and are fermions, that means they must obey the Pauli exclusion principle. With the Pauli exclusion principle comes exchange symmetry, which includes the overall asymmetric wave function.

To take a step back and think of the example with the two electrons again, how does the exchange interaction work in this case? To take a more quantum mechanical approach, will we decompose the state of the system into a spin part and a spatial part. The system can then take one of two states. Either it can go into the singlet state χ_S which has

a total spin of $S = 0$ (an asymmetric spin state) and includes a symmetric spatial wave function. The other option is the triplet state which has total spin of $S = 1$ (a symmetric spin state) and includes an asymmetric spatial wave function. These spatial wave functions are defined as:

$$|\Psi_S\rangle = \frac{1}{\sqrt{2}}[\psi_a(\mathbf{r_1})\psi_b(\mathbf{r_2}) + \psi_a(\mathbf{r_2})\psi_b(\mathbf{r_1})]\chi_S = \frac{1}{\sqrt{2}}(|\mathbf{r_1r_2}\rangle + |\mathbf{r_2r_1}\rangle \tag{5}$$

$$|\Psi_T\rangle = \frac{1}{\sqrt{2}}[\psi_a(\mathbf{r_1})\psi_b(\mathbf{r_2}) - \psi_a(\mathbf{r_2})\psi_b(\mathbf{r_1})]\chi_T = \frac{1}{\sqrt{2}}(|\mathbf{r_1r_2}\rangle - |\mathbf{r_2r_1}\rangle \tag{6}$$

To gain the energies of the states, we need the wave functions to be normalized then the energies can be calculated by:

$$E_S = \langle\Psi_S|\mathcal{H}|\Psi_S\rangle = \langle\mathbf{r_1r_2}|\,\mathcal{H}\,|\mathbf{r_1r_2}\rangle + \langle\mathbf{r_2r_1}|\,\mathcal{H}\,|\mathbf{r_1r_2}\rangle \tag{7}$$

$$E_T = \langle\Psi_T|\mathcal{H}\Psi_T\rangle = \langle\mathbf{r_1r_2}|\,\mathcal{H}\,|\mathbf{r_1r_2}\rangle - \langle\mathbf{r_2r_1}|\,\mathcal{H}\,|\mathbf{r_1r_2}\rangle \tag{8}$$

The Coulomb interaction is described in the Hamiltonian $\mathcal{H}$ and ensures $E_s \neq E_T$. We can now reunite equation(7) and 8. $\mathbf{S}_1 \cdot \mathbf{S}_2$ interaction for the two different states gives, for the singlet $-\frac{3}{4}$ and for the triplet $\frac{1}{4}$ [1]. By this we gain a new Hamiltonian that can be written as:

$$\mathcal{H} = \frac{1}{4}(E_s + 3E_T) - (E_S - E_T)\mathbf{S}_1 \cdot \mathbf{S}_2 \tag{9}$$

From this we can determine that, without the unimportant constants, there are terms that contribute to the energy which can be formulated as:

$$J = \frac{E_S - E_T}{2} \tag{10}$$

This constant is called the exchange constant and with this we can rewrite the spin depend part of the Hamiltonian into:

$$\mathcal{H}^{spin} = -2J\mathbf{S}_1 \cdot \mathbf{S}_2 \tag{11}$$

Doing this for multiple spins gets tedious and therefore a general definition of the Hamiltonian forms:

$$\mathcal{H} = -2\sum_{<ij>} J_{ij}\mathbf{S}_i \cdot \mathbf{S}_j \tag{12}$$

The sums goes over all the spin pairs and the exchange constant between the two spins. This Hamiltonian is known as the isotropic Heisenberg model and is used for most

studies of the magnetic properties.

Since we took the quantum mechanical approach the spin operator $\mathbf{S}$ must be a quantum mechanical operator which can be written as: $\mathbf{S} = (S^x, S^y, S^z)$. As said before the electrons are fermions and therefore obey the Pauli exclusion principle. The spin operator can be written with Pauli matrices, $\sigma_x, \sigma_y, \sigma_z$ so that $S^x = \frac{1}{2}\sigma_x$. With this we are able to rewrite the S^x and S^y operator, and introduce the raising and lowering operators S^+, S^-.

$$S^x = \frac{1}{2}(S^+ + S^-), \tag{13}$$

$$S^y = \frac{1}{2}(S^+ - S^-) \tag{14}$$

The commutator relations of these are:

$$[S_i^z, S_j^\pm] = \pm S_i^\pm \delta_{i,j}, \tag{15}$$

$$[S_i^+, S_j^-] = 2S_i^z \delta_{i,j} \tag{16}$$

2.2.1 Zeeman interaction

Since electrons have magnetic moments, its possible to think they would interact with other magnetic fields. This is the case when we apply an external magnetic field and the interaction is called the Zeeman interaction. The Zeeman interaction is included in the Heisenberg Hamiltonian as:

$$\mathcal{H}_Z = -g\mu_B \sum_i \mathbf{B} \cdot \mathbf{S}_i = -\sum_i \mathbf{h} \cdot \mathbf{S}_i \tag{17}$$

g is the oddly named g-factor and $\mathbf{h}$ is the reduced magnetic field and is defined by $\mathbf{h} = g\mu_B\mathbf{B}$. This external field makes the spins align with the field (parallel) to minimize the energy. Since the magnetic moments of the electrons are close to each other they do also interact with each other. This effect is much weaker than the interaction with the applied field and therefore can be forgotten and the electrons can be thought of as individual. This type of magnet is called a paramagnet and the system is disordered with no magnetization without an applied magnetic field.

2.3 Frustration

Frustrated magnetism is a fairly new and active field with discussion on the definitions of many concepts such as geometrical frustration, quantum spin liquids and spin glasses which all will be introduced here. Since the geometrical frustration is the most visual topic I will start with this.[6]

Geometrically frustrated systems have lattices that cannot be ordered due to their geometry. This can be shown by the example of the antiferromagnetic Ising model on the triangular lattice:

$$\mathcal{H} = J \sum_{<ij>} S_i^z S_j^Z \tag{18}$$

J is the exchange coupling of the spins in position i and j. Since we have antiferromagnetic exchange interactions they will minimise the energy by $J < 0$. This is achieved by the spins facing in the opposite direction of their neighbors (if one is pointing $\uparrow$ its neighbours will point $\downarrow$). This cannot be done in all spin lattices as for example in the triangular lattice or the diamond chain (as azurite) seen in figure 1 (c) and (b). These are called frustrated spin systems. It is not possible for these systems to find a unique ordering pattern, which causes a large ground state degeneracy.

Frustration is a research topic where the main focus is magnetic materials where the spin system has many possible symmetries. This includes the 1D regime, 2D regime and 3D regime. The 2D regime includes systems like the triangular lattice and the kagome lattice. For the 1D regime the diamond chain is a possible example and can be seen in figure 1. The pyrochlore lattice is an example of a 3D geometrically frustrated system.
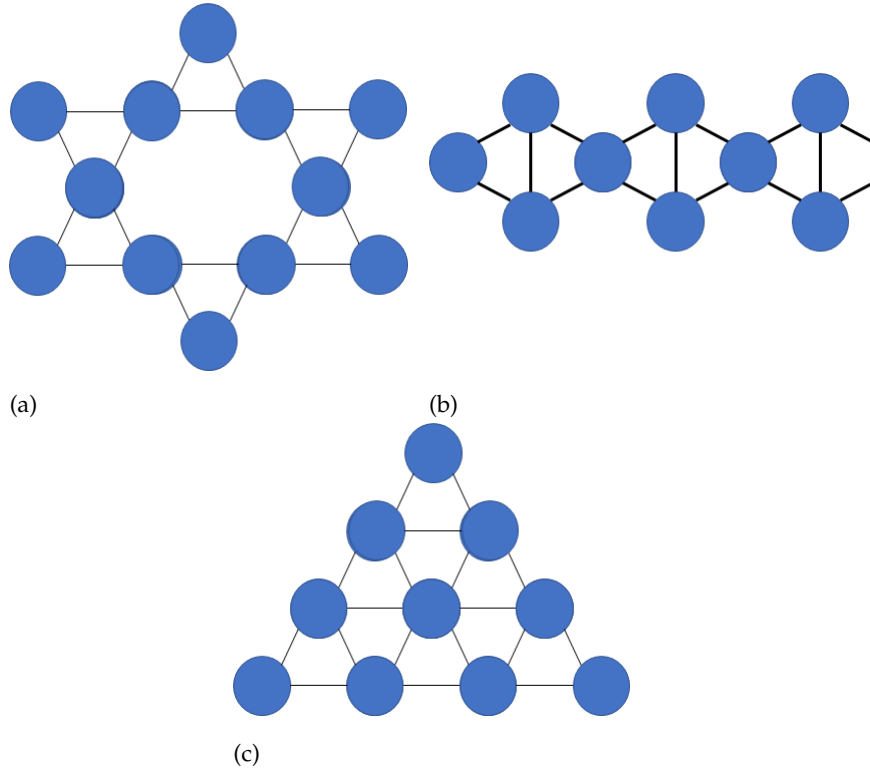
Figure 1: (a) is the kagome lattice, (b) is the diamond chain and (c) is the triangular lattice

The Ising model in the triangular lattice looks like it must be fully frustrated, which changes if one of the spins changes into a Heisenberg antiferromagnetic interaction instead. $\mathcal{H} = J \sum_{<ij>} S_i \cdot S_j$, where $S_i = (S_i^x, S_i^y, S_i^z)$ is an isotropic spin operator. This case is different from the Ising since the Heisenberg triangular lattice does order at 0 K in the 120° three-sublattice structure [6]. The ground state is when all the spins have 120° angle to its neighbour, and this will create the three sublattices. The thing is that this ordering also occurs in the quantum $S = 1/2$ system and classical spins. These systems will still be frustrated but changes the discrete spins to isotropic spins.

Geometrically frustrated magnets are most easily found by the dependence on temperature T of their magnetic susceptibility χ. It is convenient to consider plots of χ^{-1} vs T, which at high temperature have the linear form:

$$\chi^{-1} \propto T - \Theta_{CW}, \tag{19}$$

Where the sign and strength of the interaction depends on the Curie-Weiss constant Θ_{CW}. For the antiferromagnet the Curie-Weiss constant is negative. Frustration and magnetic order are seen as a sharp kink in χ, which happens below the Néel temperature, $T_N \approx |\Theta_{CW}|$. Geometrically frustrated systems do not have this sharp change below the Néel temperature due to the interaction strength. Geometrically frustrated systems have an extended paramagnetic phase which goes to temperatures $T \ll \Theta_{CW}$.

Most research on geometrically frustrated systems has a focus on quantum spin liquids (QSL). [6] QSL systems are so frustrated that they never order, which is why they are interesting. In condensed matter physics the QSL is something to be sought after since the QSL states are highly correlated and should not have magnetic long range order or no spontaneous symmetry breaking at any temperature due to the strong quantum fluctuations. QSL are a type of frustrated system in which the frustration comes from exotic forms of complex order breaking SU(2) symmetry but still support Goldstone modes, and therefore can be understood by semiclassical (spin wave like) approximations. There are two different types of QSL, the first is Valence Bond Crystals (VBC) systems and the other is Radionance Valence Bond (RVB) systems.

We need to take a step back and start introducing valence bonds. A valence bonds is a bond where in a singlet state that connects two $S = \frac{1}{2}$ spins at the positions of a and b in a lattice, and hereafter will be called $|ab\rangle$. The valence bond in this state is where the energy is minimized of the antiferromagnetic Heisenberg coupling between the two spins, $\langle ab| \, \mathbf{S}_a \cdot \mathbf{S}_b \, |ab\rangle = -\frac{3}{4}$. The valence bond configuration is a tensor product of all the different valence bonds from all the sites in the lattice, which means in a case of a N-site lattice the valence bond configuration will have the total spin $S_{tot}^2 = S_{tot}(S_{tot} + 1) = 0$. To continue lets take the simple case of the nearest-neighbor Heisenberg Hamiltonian on a lattice with coordination number z and the variation of energy per spin of the purely classical Néel state (e_{cl}) compared to the valence bond (e_{vb}) configuration. For the bipartite lattice, the energies are $e_{cl} = -\frac{z}{2}\frac{1}{4}$ and $e_{vb} = -\frac{3}{8}$, and for a 2D tripartite lattice the energies are $e_{cl} = -\frac{z}{2}\frac{1}{8}$ and $-\frac{3}{8}$.

For the classical picture the best lattices will be in the square lattice, exact diagonalization (will be explained in section 4.1) with finite-size scaling, will have Néel order at $T = 0$ and in dimensions $D > 1$. The classical result is renormalized by spin-waves. Valence bond configurations are in favor in cases of Heisenberg models on lattices such
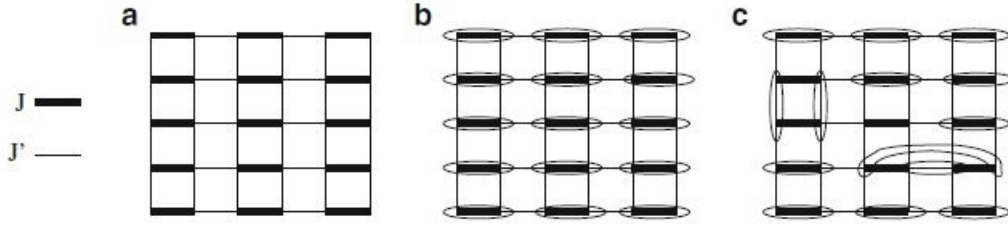
Figure 2: (a) weakly coupled dimers in a Heisenberg model. (b) The limit of J' = 0 the trivial ground state is a product of spin singlet states. (c) For small J' but non zero, other valence bond configurations appear.

as 2D kagomé and 3D pyrochlore. These systems do not develop long ranged Néel order at $T = 0$. Only in rare cases is a VB configuration an exact eigenstate of the Hamiltonian [8]. In these cases the effect of the fluctuations of these valence bond configurations are essential to find the true ground states.

VBC can also be divided into two groups. In the first group, the optimal valence bond pattern for energy is unique, which respect to all the lattice symmetries and each cluster fits into the unit cell of the lattice. In the second group, each single cluster involves spins from a number (minimum two) of unit cells, multiple valence bond patterns, which are related by symmetry, are degenerate. In case of the second group, VBC formation spontaneously breaks some discrete lattice symmetries. A system of weakly coupled dimers, as in Fig 2 (a), is an example of group 1 while the frustrated Heisenberg model of (b) is an example of group 2. The two groups are pretty similar.

It is important to remember that VBCs do not break any continuous symmetries and do not have gapless Goldstone modes. This implies that materials of this type do not melt like conventional solids, since they has a protection of the gap in the excitation spectrum. Strong thermal fluctuations are expected to restore the broken symmetry in group 1. This gives rise to one or more finite temperature phase transitions.

As said above the central idea of VBC is that a small number of spatially ordered VB configurations are favored at $T = 0$. In some geometries, however this is far from evident, and the nearest-neighbor Heisenberg model on the kagomé lattice provides one of the most straightforward examples which nevertheless contains some of the most complex physics.

In the case where there is no preferred ordering pattern, the ground state will be weighted of the same order of magnitude over many different valence bond configurations. From

9

this picture of an RVB liquid, one may anticipate the following properties:

- such a system has no LRO in any spin, dimer or higher order correlation functions. It is a true liquid.

- The absolute ground state wave function is the most stable superposition of VB configurations.

- RVB liquid ground state wave function contains long exchange cycles between different VB configurations.

To get more information on these topics look in [8] chapter 1 and 2.

3 Neutron scattering

A experimental technique that is used to study the structure and dynamics in soft, hard and biological matter and materials. This technique is one of the most versatile experimental methods and is reminiscent of X-ray. It takes a longer time to execute but it gives more information about the properties on the material. One of these is the magnetic properties. [15][5]

3.1 Neutron scattering basics

Neutron scattering uses a reactor or a source that creates neutrons, which is getting transported by neutron guide to hit the sample. Either it will get reflected or penetrate the sample after which the neutrons will be absorbed by the detectors.
The mass of the neutron is

$$m_n = 1.67493 \cdot 10^{-27} kg. \tag{20}$$

So the neutron is a little heavier than the proton which it is sharing the nucleus of the atoms with. Neutrons are not usually found free in nature, which means they decays. The lifetime of a neutron is $\tau = 886s$ hereafter it will decay into a proton, electron and an anti-neutrino. Luckily the lifetime of neutrons is a lot longer than the time it uses in a neutron experiment.
As said before, with neutron scattering it is possible to investigate the magnetic properties of the material. This is because the neutron has a magnetic moment but is electrically neutral.

$$\mu = \gamma \mu_N \tag{21}$$

where $\gamma = -1.91304$ is the neutron magnetogyric ratio and the nuclear magneton is given by $\mu_N = \frac{e \cdot \hbar}{2 \cdot m_p} = 5.05078 \cdot 10^{-27} \frac{J}{T}$. The neutrons spin is $s = \frac{1}{2}$ and is coupled anti parallel to the magnetic moment. I will primarily go through magnetic scattering.
The neutrons are created in either a fission reactor from for example uranium or from a spallation source, which is where neutrons are produced from a heavy element that is bombarded with high-energy particles, typically accelerated protons. From here it travels through a guide concentrated as a beam. The neutron beam has a flux of:

$$\psi = \frac{\text{number of neutrons impinging on a surface per second}}{\text{surface area perpendicular to the neutron beam direction}} \tag{22}$$

11

and is usually given in units of $\frac{n}{cm^2 \cdot s}$. The flux needs to be taken into consideration since the difference of the setups of different neutron facilities goes from 10^4 to $10^{10} \frac{n}{cm^2 \cdot s}$

The next part of the experiment is the scattering from the sample. The scattering cross section is the ability of the system to scatter neutrons. The total scattering cross section is given by:

$$\sigma = \frac{1}{\psi} \cdot \text{number of scattered neutrons per sec} \tag{23}$$

Where the unit is given in area. The scattering cross section section used depends on the sample volume, V. The most important thing is the angular dependency of the scattered neutrons. A simple way to imagine this is to follow the neutron beam. The incoming neutron, which will be called $\mathbf{k}_i$ for initial neutron wave vector, hits the sample and scatters. After the beam has been scattered we call it $\mathbf{k}_f$ for final vector. The difference between $\mathbf{k}_i$ and $\mathbf{k}_f$ is the scattering vector $\mathbf{q}$.

$$\mathbf{q} = \mathbf{k}_i - \mathbf{k}_f \tag{24}$$

Another important concept is the energy transfer of the scattering process. If the energy of the incoming neutrons is not the same as the neutrons that hit the detectors it is called inelastic scattering. When doing inelastic scattering, it is often preferred to scan over the incoming or outgoing energies to map out parts of $(\mathbf{q}, \omega)$. The energy transfer is called $\hbar\omega$ and the neutron initial energy E_i and final energy E_f which is defined as:

$$\hbar\omega = E_i - E_f = \frac{\hbar^2}{2m_n}(|k_i|^2 - |k_f|^2) \tag{25}$$

Since all the neutrons in the beam do not have the exact same angle when they hit the sample, they will scatter in a solid angle $d\Omega$ with the final wave vectors $\mathbf{k}_f$. This is shown in figure 3. This means that when the detector absorbs the neutrons they will be measured in the partial differential scattering cross section.

$$\frac{d^2\sigma}{d\Omega dE_f} = \frac{1}{\Psi} \cdot \frac{\text{No. of neutrons scattered per sec into } d\Omega \text{ with energies } [E_f; E_f + dE_f]}{d\Omega dE_f} \tag{26}$$

Sometimes one would be interested in counting the neutrons and ignore the energy of the neutrons, this can be acquired by the differential scattering cross section:

$$\frac{d\sigma}{d\Omega} = \int \frac{d^2\sigma}{d\Omega dE_f} dE_f \tag{27}$$
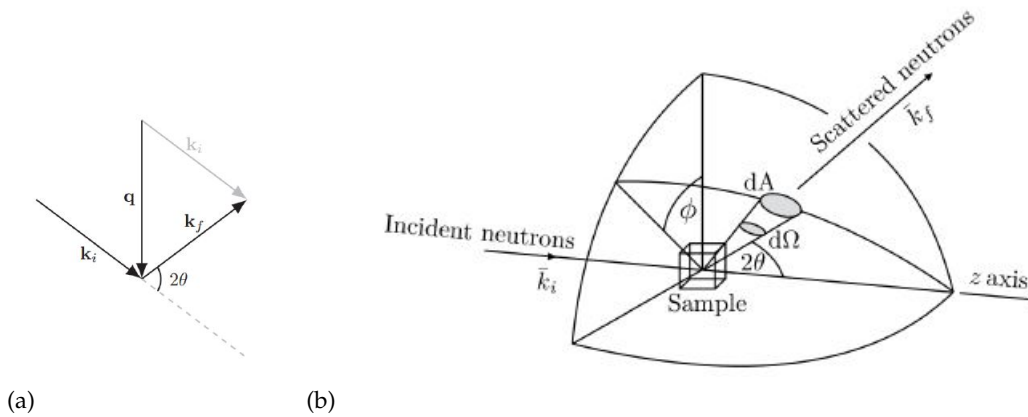
12

Figure 3: (a) Illustration of scattering vector $\mathbf{q}$ as defined via the incomming- and outgoing wave vector $\mathbf{k}_i$ and $\mathbf{k}_f$. (b) An illustration of the scattering geometry. The incoming neutrons, labeled $\mathbf{k}_i$, scatter at the center of the sphere with the scattering angle 2Θ and azumital angle$^\circ$. The neutrons scattered into the solid angle element $d\Omega$ (or detector area dA) are labeled with $\mathbf{k}_f$.[15]

If one simply counts the total number of neutrons scattered, this will again be quantified by the total scattering cross section.

 The neutrons interact with the material system but only weakly and can be thought of as a weak perturbation. This gives a small change that causes the quantum state to turn into another quantum state but the states are still intact. This means that Fermi's golden rule is a good approximation for this case. This is done by considering the neutron as a plane wave that interacts with the state of the system. It is also assumed that the wave goes unchanged through the system. The wave interacts with the potential and is scatted.

Fermi's golden rule will then give us:

$$\sum_{\substack{\mathbf{k_f} \\ \text{in } d\Omega}} \mathbf{W}_{\mathbf{k}_i, \lambda_i \to \mathbf{k_f}, \breve{\mathbf{f}}} = \frac{2\pi}{\hbar} |\langle \mathbf{k}_i, \lambda_i | V | \mathbf{k}_f, \lambda_f \rangle|^2 \rho \mathbf{k}_f \tag{28}$$

where $\mathbf{k}_i, \mathbf{k}_f$ is the incoming and outgoing wavevector, λ_i, λ_f is the initial and final state of the sample, $W_{\mathbf{k}_i, \lambda_i \to \mathbf{k}_f, \lambda_f}$ is the transition rate, and $\rho_{\mathbf{k}_f}$ is the density of final momentum states in $d\Omega$, found by box normalising the system. In [14] the result for the

13

differential cross section is found to be:

$$\left(\frac{d\sigma}{d\Omega \, dE}\right)_{\lambda_i \to \lambda_f} = \frac{|\mathbf{k}_f|}{|\mathbf{k}_i|}\left(\frac{m_n}{2\pi\hbar}\right)^2 |\langle \mathbf{k}_i, \lambda_i | V | \mathbf{k}_f, \lambda_f \rangle|^2 \delta(\hbar\omega + E_i - E_f) \qquad (29)$$

In actual experiments we collect all the finals states λ_f, sum over them, and hold the initial state fixed λ_i instead of measuring the scattering from the initial to the final. The fixed initial state is obtained by an average over all initial states [14]. This average is performed by multiplying the probability of the system that we scatter off, is in each of the initial state, ρ_{λ_i}, and then sum all the initial states. ρ_{λ_i} is given by the Boltzmann distribution for each initial state at temperature T:

$$\rho_{\lambda_i} = \frac{1}{Z}\exp\left\{-\frac{E_{\lambda_i}}{k_B T}\right\}, \qquad (30)$$

$$Z = \sum_{\lambda_i}\exp\left\{-\frac{E_{\lambda_i}}{k_B T}\right\}, \qquad (31)$$

Where Z is the partition function. The total partial differential scattering cross section in its final form is given by:

$$\left(\frac{d^2\sigma}{d\Omega dE}\right)_{\lambda_i \to \lambda_f} = \frac{|\mathbf{k}_f|}{|\mathbf{k}_i|}\left(\frac{m_n}{2\pi\hbar}\right)^2 \sum_{\lambda_i}\rho_{\lambda_i}|\langle \mathbf{k}_i, \lambda_i | V | \mathbf{k}_f, \lambda_f \rangle|^2 \delta(\hbar\omega + E_i - E_f) \qquad (32)$$

3.2 Magnetic scattering

To the magnetic dipole moment in neutrons makes them able to interact with the variations of the magnetic fields inside the material. The electronic magnetic moment is often the source that generates the external magnetic field that the neutrons are interaction with. This can be described by the Zeeman term for a neutron interacting with this field. The derivation can be found in [14] and the result for spin only unpolarised magnetic scattering is:

$$\frac{d^2\sigma}{d\Omega dE} = (\gamma r_0)^2 \frac{|\mathbf{k}_f|}{|\mathbf{k}_i|}(\frac{g}{2}F(q))^2 e^{2W} \sum_{\substack{\alpha,\beta \\ \in x,y,z}} (\delta_{\alpha,\beta} - q_\alpha q_\beta)S^{\alpha,\beta}(\mathbf{q},\omega) \qquad (33)$$

Where $r_0 = \frac{e^2}{m_e c^2}$ is the classic electron radius, g is the Landé g-factor, $F(\mathbf{q})$ is the magnetic form factor, and e^{-2W} is the Debye-Waller factor which contains the local thermal vibrations in the lattice. The term $\Sigma_{\alpha,\beta}(\delta_{\alpha,\beta} - q_\alpha q\beta)$ is to make sure that only spin com-

ponents that are perpendicular to the scattering vector is contributing to the partial differential cross section. The last term in the equation is the dynamical correlation function. Many of the components are either constants or depends on the experimental setup.

Theoreticians will often be looking at the dynamical correlation function, and not the rest of the cross sections, since it captures relevant dynamics of the sample that do not depend on the experimental setup. It will be to much work to be calculate the full cross-section with all the external factors by hand. The dynamical correlation function is defined as:

$$S^{\alpha,\beta}(\mathbf{q},\omega) = 2\pi \sum_{\lambda_i,\lambda_f} r_{\lambda_i} \left\langle \lambda_i \middle| S^{\alpha}_{-\mathbf{q}} \middle| \lambda_f \right\rangle \left\langle \lambda_f \middle| S_{\mathbf{q}^{\beta}} \middle| \lambda_i \right\rangle \delta(\hbar\omega + E_i - E_f) \tag{34}$$

Again p_{λ_i} is the Boltzmann factor and the sum goes over all the states, while the operator $S^{\alpha}_{-\mathbf{q}}$ is the spin operator after the Fourier transformation. It is defined as:

$$S^{\alpha}_{\mathbf{q}} = \frac{1}{\sqrt{N}} \sum_j S^{\alpha}_j e^{i\mathbf{q}\cdot\mathbf{r}_j} \tag{35}$$

The dynamic two-spin correlation function in $(\mathbf{q},\omega)$-space, $S^{\alpha,\beta}(\mathbf{q},\omega)$, has several names for example the dynamic structure factor or the spectral function. While we use Lehmann's representation of the dynamical correlation function in equation (34), it is also possible to convert the dynamical structure factor to be dependent on the time-dependent spin operators by:

$$S^{\alpha,\beta}(\mathbf{q},\omega) = \int_{-\infty}^{\infty} dt e^{-i\omega t} \sum_l e^{i\mathbf{q}\cdot\mathbf{r}_l} \left\langle S^{\alpha}_0(0) S^{\beta}_l(t) \right\rangle \tag{36}$$

where the brakets indicate an average over all configurations. $S^{\alpha,\beta}(\mathbf{q},\omega)$ quantifies, in a loose sense, in which direction the excitation connecting the states λ_i and λ_f points in spin-space. Thus, for instance, for $\alpha = \beta = z$ the matrix product $|\left\langle \lambda_i \middle| S^z_{\mathbf{q}} \middle| \lambda_i \right\rangle|^2$ will quantify how much weight along the z direction the scattering event from λ_i to λ_f will contribute. This can also be seen from the expression in equation (36), where the dependence is contained in the term $< S_0 * \alpha(0) S^{\beta}_l >$ representing e.g. the components of a spin wave excitation.

In unpolarised neutron scattering, where the neutrons have randomly oriented spins, one will measure all $S^{\alpha,\beta}(\mathbf{q},\omega)$ at the same time, and thus separation into individual α, β channels is not possible with this technique. Exploiting the fact that magnetic scattering

15

occurs only for spin components perpendicular to the scattering vector, one can obtain information on the spin directions in the sample using spin-polarised neutron scattering. By measuring the scattering intensities for different combinations of incoming and outgoing neutron spins, it is possible to extract information on the spin configuration in the sample. Additionally one can separate the different $S^{\alpha,\beta}(\mathbf{q},\omega)$ or some parametrization hereof into different channels, and thus analyse them separately.

For a theoretical $T = 0$ experiment the system will always be in the ground state before any excitation, and the dynamical correlation function can be simplified to read:

$$S^{\alpha,\beta}(\mathbf{q},\omega) = \sum_e M^{\alpha,\beta}_{e,\mathbf{q}} \delta(\hbar\omega + E_{gs} - E_e), M^{\alpha,\beta}_{e,\mathbf{q}} = 2\pi \langle gs| S^{\alpha}_{-\mathbf{q}} |e\rangle \langle e| S^{\beta}_{\mathbf{q}} |gs\rangle \qquad (37)$$

Here $|e\rangle$ is an excited state, $|gs\rangle$ is the ground state and $M^{\alpha,\beta}_{e,\mathbf{q}}$ is the matrix element that quantifies the probability for the ground state to scatter to a given excited state. $S^{\alpha,\beta}(\mathbf{q},\omega)$ is loosly a direction where the excitation that connects the initial and the final states is "pointing". For example the matrix product $\left|\langle\lambda_f|S^{-}_{\mathbf{q}}|\lambda_i\rangle\right|^2$ for $\alpha = \beta = z$ will show how much weight the z direction of the the scatting event is contributing. The dependence is in the term of $\left\langle S^{\alpha}_0(0)S^{\beta}_l(t)\right\rangle$, which is the components of a spin wave excitation. For the case where $\alpha = \beta$ which is often the case with the most interest, this can be rewritten as:

$$2\pi \sum_{\lambda_i} \lambda_f \rho_{lambda_i} |\langle\lambda_i| S^{\alpha_q} |\lambda_f\rangle|^2 \delta \qquad (38)$$

The method and program are described in Exact diagonalization below.

4 Exact diagonalization

RLexact is a program used to perform exact diagonalisation on finite size $s = \frac{1}{2}$ system to get eigenengeries and dynamical correlations functions.[5][13]

4.1 Exact Diagonalisation

Finding eigenvalues and -states of spin systems larger that 4 spins, $s = \frac{1}{2}$, is demanding a lot of time to calculate by hand and this is why many of the calculating tasks in condensed matter have moved to be calculated by computers. There are many different computational methods that shine and disappoint in different areas in this field. The two most used are the Quantum Monte Carlo, which in short terms shines in the thermal part of this field[24]. The other one is exact diagonalization, which will be gone through here.

Exact diagonalization focuses on zero temperature, $T = 0$ and on finding eigenstates and -values. As the name implies the method diagonalize matrices and for larger systems, pretty large matrices needs to be computed. If we take an example where a lattice system has the degrees of freedom per site is $K = 2S + 1$ where $K = 2$ and $S = \frac{1}{2}$. The dimensions in the Hilbert space will be given by the number of basis states $N_{st} = K^N$, and N is the number of spins. This means that both K and N are required to be small to modest, since this is the limitation of computational calculations. Even though it is still able to get eigenenergies and -states out of larger systems than is possible to do by hand. Exact Diagonalization uses two steps, which starts with setting up the system with its Hamiltonian and then diagonalizing the large matrices created from that. Computational calculations drawback is how much time and hardware it needs to run. This is what makes it a desirable way of getting larger matrices calculated. The diagonalization in RLexact is actually done by the Lanczos algorithm which can be found in section 4.6.

The Lanczos algorithm has been chosen is mainly because it fast and does not require too much memory to deal with large matrices. The requirement to use the standard diagonalization techniques is the CPU run-time, which scales with the number of operations, $Op \sim \mathcal{O}(N_{st}^3)$, while the memory requirement is to store the matrices created from the Hamiltonian, it goes as $Mem \sim \mathcal{O}(N_{st}^2)$. To set some numbers at the Lanczos

iterative method it goes down roughly to $Op \sim \mathcal{O}(N_{st}), Mem \sim \mathcal{O}(N_{st})$ for sparse matrices.

Since computers are binary (as before the quantum computer) the algorithm works especially well for spin-$\frac{1}{2}$ systems. Why you might ask, this is because spin-$\frac{1}{2}$ systems only have two different states the spins can be in. These states are spin up $\uparrow$ and spin down $\downarrow$ and these states can be converted into bit values of 0 or 1 as integers. The language, ANSI C, that RLexact is written in has a limit of how long unsigned integers can be of a max of 64 bits. But it is possible to save entire spin configurations in an integer and because of this save huge amount of memory and time since bit-operations are really fast.

4.2 Symmetries

Another thing that can be done to help the computational limitation is to limit the is when creating large systems with many spins, is to limit the number of basis states that needs to be calculated so the N_{st} decreases. This is done by using symmetries in the system, this makes it possible to break the Hamiltonian into smaller blocks and therefore create smaller matrices that can be diagonalized separately. Symmetries that I will use in this thesis is the translational symmetry and the mirror symmetry.
This thesis is working with the Heisenberg Hamiltonian which is defined as:

$$\mathcal{H} = \sum_{i,j} J_{ij} \overline{S}_i \overline{S}_j \tag{39}$$

4.2.1 Translation

The translational symmetry works but only on systems with periodic boundary conditions. Periodic boundary conditions are often used to approximate large or infinite systems by only looking at a small portion of the system. This is done in figure 4 a to b. For a more mathematical approach and as seen from figure 4 c to d the periodic boundary condition works as the next in the chain after the "last" will be the first in the chain, $S_{n+1} = S_0$.
The standard notation of describing the basis state is $|S_0, S_1, ...S_{n-1}\rangle$, where each spin in written in the S^z-basis. The translational symmetry then works as to move all

the spin one time to the right in a cycle such as:

$$T |S_0, S_1, ...S_{n-1}\rangle = |S_{n-1}, S_0, S_1, ...S_{n-2}\rangle \qquad (40)$$

If the translation operator is used n times S_0 will have moved through all the possible positions and have come back to the original position. Since the energy calculated from the Heisenberg Hamiltonian in equation (39) does not change due to the translation operation they commute, $[\mathcal{H}, T] = 0$.

All these states that can be found by the translation operator will be alike and therefore they can be included in a combined state. See section 4.3. For a single spin chain system, this means that the translation operator works on the system to move one unit cell at a time, which is one spin at a time. For other systems with larger unit cells, as azurite, the translation operator moves one unit cell that contains multiple spins, three in the azurite system.
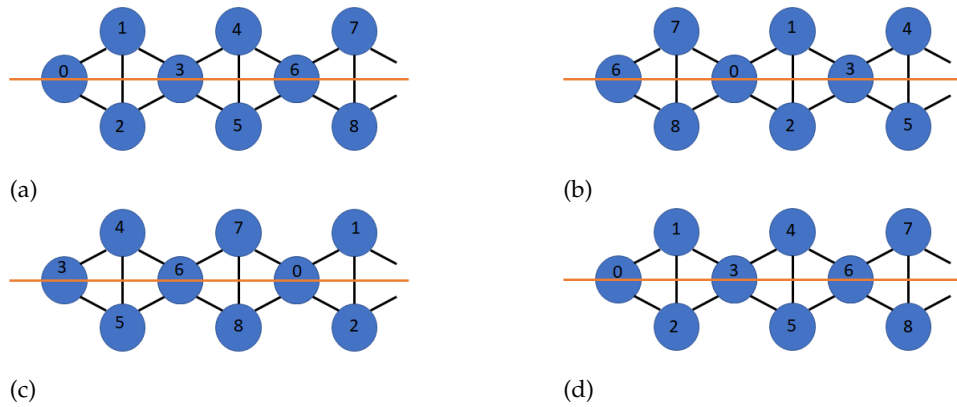

(a)

(b)

(c)

(d)

Figure 4: Diamond chain of spins. a) Starting position. b) First use of the translational operation. c) Second translation operation. d) Third translation operation and are now back where we started.

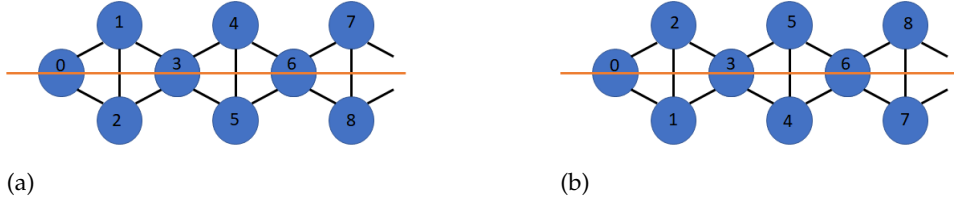(a)   (b)

Figure 5: (color plot) Nine spins in diamond chain model with symmetries where the orange line represent the mirror line. From (a) to (b) has the mirror symmetry been in use.

4.2.2 Mirror

Azurite is considered a 1D diamond chain, which is constructed of triangles. As it is shown in figure 5 this means that we can use another symmetry that is called mirror symmetry. Spins in the mirror plane does not get affected by the symmetry operator $\mathbf{M}$ and stays the way they are. When the mirror operator works on the system, spins on each sides of the plane swap places. As for the translation operator can this be shown by the following formula.

$$M \ket{S_0, S_1, S_2, S_3, S_4, S_5} = \ket{S_0, S_2, S_1, S_3, S_5, S_4} \tag{41}$$

States in the azurite system will be able to use the mirror operator two times before the state will become the same again ($\mathbf{M}^2 = I$). Since the Heisenberg Hamiltonian will look at two spins at a time and all the spins in azurite are connected with their neighbors the swap does not affect the energy, therefore the swap happens with eigenvalues 1(symmetric) or -1 (antisymmetric). The mirror operator and the Heisenberg Hamiltonian commute $[\mathcal{H}, M] = 0$. These states can also be combined into a single states .

4.3 Uniques

Uniques states will be referred as uniques from now. Uniques are states that with use of the symmetries can create a single state that represent many different states. To save as much memory as possible, RLexact is using these uniques represented in the z-basis as bit values translated to a single integer. This way to store spin systems allocates 64 bits to each unique. An example of this for $N = 1$, 1 represent the spin up $\ket{\uparrow}$ and 0 represent spin down $\ket{\downarrow}$. For N = 3 spins:

$$\ket{\uparrow\downarrow\uparrow} = \ket{010} = \ket{2} \tag{42}$$

The last integer is then saved as a unique. These uniques can be created by taking the "first" state $|000\rangle$ and then use symmetry operations on this state to create the other uniques.

4.4 Momentum states

There are two different ways to look at the system, one is in the position space where the spins are placed in, or in the momentum space where the spins has each a momentum vector. These two spaces are easily to come from one to the other, from position space to momentum space is with the Fourier transformation and the opposite way by the inverse Fourier transformation.

RLexact is working with momentum states $|\Psi_k\rangle$. When symmetries are applied on momentum states it will by definition be an eigenstate to the symmetry operator:

$$T |\Psi_{k,M}\rangle = e^{-ik} |\Psi_{k,M}\rangle , \tag{43}$$

$$M |\Psi_{k,M}\rangle = e^{-iM} |\Psi_{k,M}\rangle \tag{44}$$

Where T is the translational symmetry and M is the mirror symmetry. Since translation symmetry is periodic it requires that $T^{r_i} = 1$, where r_i is the number of translations a unique has in the period, with the allowed momenta used for the eigenvalue equation $k = \frac{2\pi q}{N}$, with $q = 0, 1, ..., N-1$. The states with different q's will then be able to form their own blocks in the Hamiltonian, seen in figure 6 to be diagonalized separately. The uniques with all the symmetries used for a single state in the Ising basis will be given as:

$$|u_{q,i}\rangle = \frac{1}{\sqrt{N_i}} \sum_{r=0}^{N_i-1} \sum_{b=0}^{1} \exp\left\{ \frac{2i\pi qr}{N} \right\} (-1)^b T^r M^b |u_i\rangle \tag{45}$$

$$N_i = \frac{N^2}{R_i} \tag{46}$$

Where N_i is a normalized constant by N the system size and R_i the periodicity of the given unique.

This normalization constant is to catch the multiple times the same unique will be counted in the sum.

Figure 6: Example of a block Hamiltonian from code validation in chapter 6

4.5 Hamiltionian in momentum basis

Since we have converted the eigenstates into momentum basis, we must construct the Hamiltonian in the same basis of momentum states. The Hamiltonian will then work on the uniques that are also written in a basis of the momentum states $\left|u_{q,i}\right\rangle$ and since the symmetries commute with the Hamiltonian which gives:

$$\mathcal{H}\left|u_{q,i}\right\rangle = \frac{1}{\sqrt{N_i}} \sum_{r=0}^{N_i-1} \sum_{b=0}^{1} e^{\frac{2i\pi qr}{N}} \mathcal{H} - 1^b T^r M^b \left|u_i\right\rangle \tag{47}$$

$$= \frac{1}{\sqrt{N_i}} \sum_{r=0}^{N_i-1} \sum_{b=0}^{1} e^{\frac{2i\pi qr}{N}} (-1)^b T^r M^b \mathcal{H} \left|u_i\right\rangle \tag{48}$$

$$\tag{49}$$

Since each unique consists of states where each has a coefficient c_L the Hamiltonian we have:

$$\mathcal{H}\left|u_{q,i}\right\rangle = \frac{1}{\sqrt{N_i}} \sum_{r=0}^{N_i-1} \sum_{b=0}^{1} \sum_{l} e^{\frac{2i\pi qr}{N}} (-1)^b T^r M^b c_l \left|u_{q,i,l}\right\rangle \tag{50}$$

4.6 Lanczos algorithm

The Lanczos algorithm is used to make the load of computations lighter when diagonalizing the Hamiltonian that has been set up by the user. This is done by a so called iterative power method and is known for converging fast for extreme eigenvalues[5]. Finding eigenvalues of large matrices is how, many of the iterative method are designed, this is also the case for the Lanczos algorithm, which is based on the Krylov space, which is a subspace of the Hilbert space. I will not go into describing the Krylov space, a description can be found in [5]. The description of the Lanczos algorithm is

based on [5][24].

When the Lanczos algorithm starts, it will make an orthogonal basis by linear com-
binations of Krylov space vectors. This is done to make sure that the Hamiltonian for
the system is tridiagonal in this basis. The lowest and highest eigenenegies is where
the algorithm starts, and wher it is most accurate[5], the further in it goes the less ac-
curate it gets. This is done by transforming the hermitian Hamiltonian matrix of size
LxL, into a smaller tridiagonal matrix of size MxM . This tridiagonal matrix can then
be diagonalized to gain the eigenvalues and eigenstates by the same standard routines
as before. It is much faster to diagonalize a tridiagonal matrix than the "normal" and
larger matrices. Not only is speed gained by transforming the matrices into the smaller
tridiagonal but also bits of ram to "hold" the matrices of the projected Hamiltonian in
the smaller subspace MxM. The size of M can be in the order of tens to hundreds before
the convergence has been reached. The smaller the system the smaller the matrix and
the closer to the exact solution the Lanczos algorithm will be[24]. The Lanczos imple-
mented in RLexact is using normalized vectors and will be described here, and shown
in figure 7.

$$|\Phi_1\rangle = \frac{\mathcal{H}|\Phi_0\rangle - a_0|\Phi_0\rangle}{N_1} \tag{51}$$

$$\tag{52}$$

N_1 is a normalization constant. a_0 is a constant obtained by taking the inner product
with $|\Psi_0\rangle$ on each side $a_o = \langle\Psi_0|\mathcal{H}|\Psi_0\rangle$. The first step is constructing the Lanczos basis
by choosing a random and normalized state $|\phi_0\rangle$ with the only condition that it cannot
be orthogonal to the ground state of $\mathcal{H}$. This means that $|\phi_0\rangle$ will be used as the first
Lanczos vector in the newly made basis. If the matrix describing the Hamiltonian is of
size (LxL), that means that the vector will have the dimensions $(Lx1)$, which is shown
in figure 7. The next state is then given by:

$$|\phi_1\rangle = \frac{1}{N_1}(\mathcal{H}|\phi_1\rangle - a_1|\phi_1\rangle - N_1|\phi_0\rangle) \tag{53}$$

Where N_1 is a normalization constant. The a_1 constant is obtained by calculating the
inner product with $|\Phi_1\rangle$ on each side of $\mathcal{H}$ to obtain $a_0 = \langle\Phi_0|\mathcal{H}|\Phi_0\rangle$. By constructing
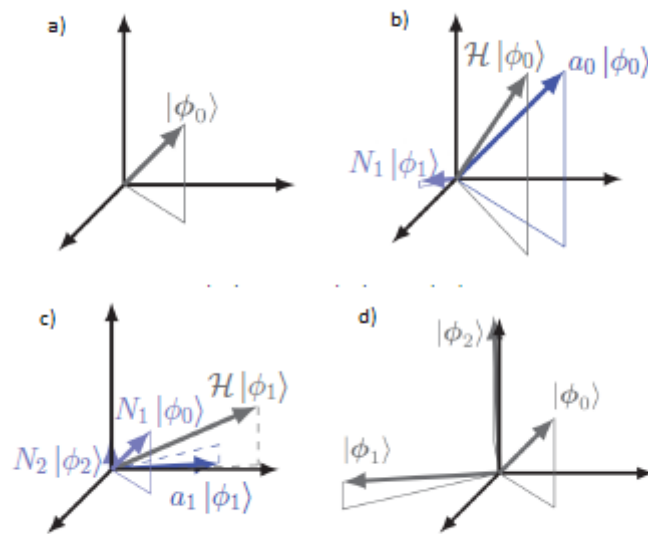
23

Figure 7: (a) Step 0: Choose arbitrary normalized state $|\phi_0\rangle$. (b) Step 1: Construct state $|\phi_1\rangle$ from $|\phi_0\rangle$.(c) Step 2: Construct state $|\phi_2\rangle$ from $|\phi_0\rangle$ and $|\phi_1\rangle$.The resulting three orthonormal vectors $|\phi_0\rangle$, $|\phi_1\rangle$ and $|\phi_2\rangle$. From [5]

the vector $|\Phi_1\rangle$ this way it is made orthogonal to Φ_0, as seen in figure 7 b. After this is done all that is left is to add it to the basis. The next state is then obtained by:

$$|\Phi_2\rangle = \frac{1}{N_2}(\mathcal{H}|\Phi_1\rangle - a_1|\Phi_1\rangle - N_1|\Phi_0\rangle) \tag{54}$$

As before N_1, N_2 are normalization constants. The parameter $a_1 = \langle\Phi_1|\mathcal{H}|\Phi_1\rangle$ is there to ensure that the state $|\Phi_2\rangle$ is orthogonal to $|\Phi_1\rangle$ as before and is also hereafter added to the basis. This is shown in figure 7c. This means that the basis now contains three orthogonal basis vectors illustrated in figure 7 (d).

The steps from here is "just" reruns of the above steps to the $(i+1)$th Lanczos vector, the maximum number of Lanczos vectors is $i = M$:

$$|\Phi_{i+1}\rangle = \frac{1}{N_{i+1}}(\mathcal{H}|\Phi_i\rangle) - a_i|\Phi_i\rangle - N_i|\Phi_{i-1}\rangle) = \frac{|\gamma_{i+1}\rangle}{N_{i+1}}, 1 \leq i \leq M \tag{55}$$

Here $|\gamma_{i+1}\rangle$ is simply the generated state before normalization. The constants are found via:

$$a_i = \langle\Phi_i|\mathcal{H}|\Phi_i\rangle \tag{56}$$

$$N_i = \langle\gamma_i|\gamma_i\rangle \tag{57}$$

Another memory saving feature of the Lanczos algorithm's design is that it only needs the two previous Lanczos vectors to generate the next. This means that it only needs to have space for three Lanczos vectors at a time, but it does still need to save all the constants of a_i, N_i. To come to the convergence of the Lanczos algorithm it will keep constructing new states $|\Phi_{i+1}\rangle$ that are orthogonal to the last two previous states $|\Phi_i\rangle$ and $|\Phi_{i-1}\rangle$. This means that the newly constructed state $|\Phi_{i+1}\rangle$ is also orthogonal to all previous states $|\Phi_k\rangle$ for $k < i-1$. This can be proven by constructing $|\Phi_4\rangle$ and also showing that it is orthogonal to $|\Phi_0\rangle$, $|\Phi_1\rangle$, this can then be done for the next state until we come to the last state. This can be shown in a general form:

$$\langle\Phi_{i+1}|\Phi_k\rangle = \frac{1}{N_{i+1}}(\langle\Phi_i|\mathcal{H}|\Phi_k\rangle - a_i\langle\Phi_i|\Phi_k\rangle - N_i\langle\Phi_{i-1}|\Phi_k\rangle) \tag{58}$$

$$= \frac{1}{N_{i+1}}(\langle\Phi_i|\mathcal{H}|\Phi_k\rangle) \tag{59}$$

$$= \frac{1}{N_{i+1}}(N_{k+1}\langle\Phi_i|\Phi_{k+1}\rangle + a_k\langle\Phi_i|\Phi_k\rangle + N_{k-1}\langle\Phi_i|\Phi_{k-1}\rangle) = 0 \tag{60}$$

This shows that any state $|\Phi_{i+1}\rangle$ is orthogonal to all previous states by using the last part of eq. (55) and made it possible to obtain a expression for $\mathcal{H}|\Phi_k\rangle$. It is possible to terminate at a given iteration, lets say $i = M$ by setting $N_{M+1} = 0$. The elements of the Hamiltonian will then be given by:

$$\langle\Phi_{i-1}|\mathcal{H}|\Phi_i\rangle = \sqrt{N_i} \tag{61}$$

$$\langle\Phi_i|\mathcal{H}|\Phi_i\rangle = a_i \tag{62}$$

$$\langle\Phi_{i+1}|\mathcal{H}|\Phi_i\rangle = \sqrt{N_{i+1}} \tag{63}$$

Even after having created M Lanczos vectors from projections of the original (LxL) Hamiltonian onto the new basis of Lanczos vectors creating a tridiagonal (MxM) matrix, $\mathcal{H}_M$:

$$\mathcal{H}_M = Q^\dagger \mathcal{H} Q \tag{64}$$

where Q is a unitary transformation matrix whose columns are the Lanczos vectors,

$$Q = [|\Phi_0\rangle, |\Phi_1\rangle, ..., |\Phi_M\rangle] \tag{65}$$

The smart thing of the tridiagonal matrix is that the eigenvalues and -vectors gained by it converges to the eigenvalues and -states of the original Hamiltonian the more Lanczos vectors that are added, and it is done with the standard routines as if it was a "normal" matrix.

The implemented Lanczos algorithm inside RLexact this is done with a tridiagonal QL algorithm with implicit shifts adapted from the book *Numerical Recipes in C*[20]. I will not go through this algorithm but to understand how RLexact is doing the diagonalization. Instead of using the last M vector as a stopping criterion, RLexact uses a dynamic stopping criterion which is based on the Ritz vector, $\langle r|r\rangle$. The Ritz is a vector that is defined as the lowest energy eigenvector for a certain subspace in the Hamiltonian, which comes from the Lanczos algorithm that through Exact Diagonalization approximate the lowest energy eigenstate.[24]

$$|r\rangle = Q|\psi_0\rangle \tag{66}$$

As for Lanczos vectors converges as more Lanczos vectors that are added to the basis, so does the Ritz vector that converges towards the true eigenvector. In RLexact, for each iteration of the Ritz vector, the energy difference between the iterations are

then evaluated. The algorithm will continue until a trigger terminates the algorithm. The trigger will go off when the energy change between the iterations becomes small (under a value we set), this means that the latest iteration did not improve the the the approximation of the true eigenvalue. All the Lanczos vectors should now be orthogonal but due to numerical truncation errors each iteration contributes to lowering the Ritz value. Loss of orthogonality is not something we want to occur in the algorithm and therefore it is not advisable to have a higher Ritz value than necessary. All of the calculations in this thesis is done with a Ritz convergence value of 0.0000001.

The last thing that should be mentioned about the Lanczos algorithm is that it cannot find more than one member of a degenerate multiplet, due to the construction of the Lanczos basis in the Krylov space[5]. The Lanczos algorithm can find some of the linear combinations that are required to find the states, which depends on the starting state $|\Phi_0\rangle$. This means that it is hard for the exact diagonalization using the Lanczos algorithm to calculate thermodynamics properties, since it may miss some states in the partition function.

4.7 Dynamical correlation functions

One thing that exact diagonalization does that something like Quantum Mondo Carlo does not is that exact diagonalization is able to calculate dynamical correlation functions directly and does not need extra time to do the advanced analytical continuations that Quantum Mondo Carlo would. Measurements of the dynamical correlation function is found in the partial differential scattering cross section of inelastic neutron scattering as described in chapter 3. Being able to numerically calculate the dynamical correlation function and with this being able to compare with experimental research is really useful and makes exact diagonalization interesting.

The dynamical correlation function for one-dimensional at $T = 0$ is:

$$S^{\alpha,\beta}(\mathbf{q},\omega) = \sum_e M^{\alpha,\beta}_{e,\mathbf{q}}\delta(\hbar\omega + E_{gs} - E_e) = \sum_e \langle e| S^{\beta}_{-\mathbf{q}} |gs\rangle \langle e| S^{\alpha}_{\mathbf{q}} |gs\rangle \delta(\hbar\omega + E_{gs} - E_e)$$

(67)

where $[\alpha, \beta] \in [x, y, z]$. The operator $S^{\alpha}_{\mathbf{q}}$ is the Fourier transform of the spin operator:

$$S^{\alpha}_{\mathbf{q}} = \frac{1}{\sqrt{N}} \sum_{j=0}^{N-1} e^{\frac{2\pi i q j}{N}} S^{\alpha}_j$$

(68)

27

N is the number of spins and the sum runs over all spin sites.

I will end it here since this is not a part of this thesis.

4.8 Overview of RLexact

After understanding the concepts RLexact is build on, exact diagonalization with the Lanczos algorithm, I will go roughly through how RLexact works.

Firstly the way to communicate with RLexact: We need to have a *header file* which contains all the information needed to run a simulation of a given material or system. The information in this file contains number of spins, symmetries, couplings, coupling strengths, how the symmetries work on the system, each coupling strength and lastly where each spin is coupled and with what strength. All this is in table 1. Firstly, the basic properties of the system are presented, which are the number of spins, the number of couplings, the three coupling strengths ($J_z, J_\perp = \frac{J_x + J_y}{2}, J_a = \frac{J_x - J_y}{2}$) and the number of symmetries. For azurite this is one translational symmetry, one mirror symmetry and the identity. The maximum and the minimum magnetisation to diagonalize is also given in the file. Only the positive magnetization is required due to the symmetry in magnetization

RLexact will use masks to gain the same outcome as using the raise/lower method. RLexact is using three different masks, they are called AND, AND NOT and OR. The OR mask could use the unique above giving the mask $|001\rangle$. OR will then compare the states and raise the 0 to a 1 if there is a 1 present at the spot in the state.

$$|101\rangle \, OR \, |001\rangle = |011\rangle \tag{69}$$

AND and AND NOT are both operations that can lower the spins. These work this way:

$$|011\rangle \, AND \, |110\rangle = |011\rangle \, ANDNOT \, |001\rangle = |010\rangle \tag{70}$$

In this way RLexact can create uniques with masks instead of spin operations.

The information about translational symmetry is input into the program simply by stating which spins are transferring to which by the symmetry operator. Prior to this, the spins in the system are numbered from 0 to $N-1$ and since azurite is built of monomers and dimers each spin will move by 3 places ($\overline{S}_i \rightarrow \overline{S}_{i+3}$) see figure 4. The information of the mirror symmetry will then swap spins in the dimers. The first symmetry vector in table 1 is the identity.

28

Variable	Value
Number of spins	6
Number of couplings	10
Number of coupling strengths	3
Number of custom symmetries	3
M start	0
M end	1
Custom symmetries	(0 1 2 3 4 5)
	(3 4 5 0 1 2)
	(0 2 1 3 5 4)
Coupling strength vector	$J_1 =$(1.337 1.337 0)
	$J_2 =$(2.845 2.845 0)
	$J_3 =$(0.597 0.597 0)
	$J_M =$(0.398 0.398 0)
Coupling vector	(0 1 0)
	(0 2 2)
	(1 2 1)
	(1 3 2)
	(2 3 0)
	(3 4 0)
	(3 5 2)
	(4 5 1)
	(4 0 2)
	(5 0 0)

Table 1: Selected parameters in the header file for RLexact for $N = 6$ with the coupling strength vectors from the article Jeschke [7], calculated from K to meV.

5 Azurite background

From azurite's chemical structure, seen in figure 8 (b), it is easy to see where the diamond chain model comes from, seen in figure 8 (a). The points used in the models comes from the spins in CU_2 (S = $\frac{1}{2}$) The experimental data that are used to describe azurite suggest the coupling constants to be antiferromagnetic and this will cause the system to be frustrated. As described in section 2.3. Since the diamond chain has been proposed as the model for Azurite it has been used greatly to try to find the exchange constants for the mineral. Which usually is described by the Hamiltonian of Heisen-

berg:

$$H = J_1 \sum_{i=1}^{L/3} [S_{3i} \cdot S_{3i+1} + S_{3i+1} \cdot S_{3+2} + J_2 \sum_{i=1}^{L/3} [S_{3i+2} \cdot S_{3i+3}] \tag{71}$$

$$+ J_3 \sum_{i=1}^{L/3} [S_{3i+1} \cdot S_{3i+3} + S_{3i+2} \cdot S_{3+4} - h \sum_{i=1}^{L} S_i^z$$

The biggest problem that is up for discussion is how many exchange constant there are and which atoms interacts. The most used number is three as shown in figure 8 a. and its typical by this model that all the three exchange constants are different from one another. All exchange constants will be collected in a Table 2
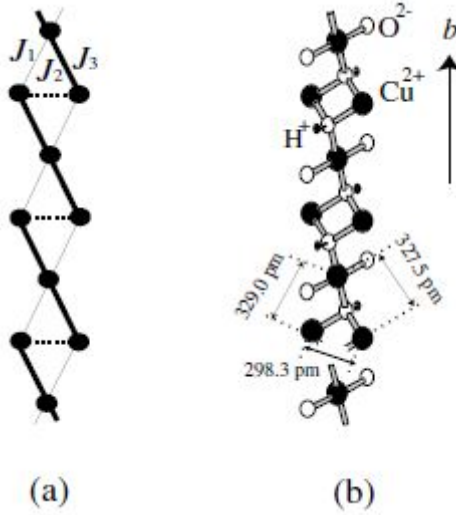

Figure 8: (a) The distorted diamond chain. (b) Schematic view of the crystal structure of the azurite $Cu_3(CO_3)_2(OH)_2$ along the b axis.[10]

5.1 Diagonalization and magnetization studies

Mikeska and Luckmann[16] investigated the phase transitions at $T = 0$ and made a phase diagram in the J_1, J_2 plane finding the ferrimagnetic phase, dimerized phase and the spin fluid phase (today known as spin liquid) in the J_1 and J_3 plane where $J_2 = 1$. It is easy to see in the numerical data if the ground state is ferrimagnetic ($M = \frac{M_s}{3}$ or $M = 0$). It is however hard to see the critical point from the spin liquid phase to the dimer phase in the numerical data. To overcome this complication they calculated the

dimer to SL intersection and looked at the energy gaps, with a method developed by Okamato [25] which uses the NNN model, illustrated in figure 9, $S = \frac{1}{2}$ to calculate the spin liquid to dimer critical points by looking at the energy gaps. This will be explained step by step here.

The ground state is usually unique and not a twofold state as for the Ising model. A twofold state can appear when the lowest lying exited state goes down, as the system size grows, and finally degenerate to the ground state as $N \to \infty$.

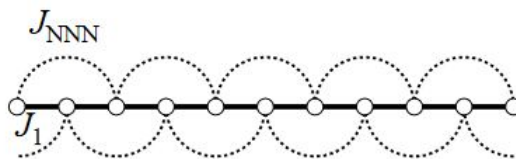In this case the ground state is two times degenerate and this consists of a linear

Figure 9: Next nearest neighbors Ising model. From [?].

combination of the ground state and the exited state as described above. From here they look at the critical point from the spin liquid to the dimer phase. When the twofold degenerate dimer state is chosen then the property $S_{tot} = 0$ for the ground state in the infinite system. Since the law of addition of the angular momentum has the same property $S_{tot} = 0$ counts for the low-lying exited state. In the spin liquid phase the low-lying exited state should be of the spin-wave type which has $S_{tot} = \pm 1$ (one magnon state).

At a point between these two phases will there be a transition where the energy has to obey both phases. The critical point will become a three-fold that has to follow these criterion [25]:

$$\Delta E_{ss}(N) < E_{st}(N) \iff (dimerstate) \tag{72}$$

$$\Delta E_{ss}(N) > E_{st}(N) \iff (spinliquidstate) \tag{73}$$

Where ΔE_{ss} is the singlet energy gap and ΔE_{st} is the triplet energy gap. These are as[25]:

$$\Delta E_{ss} = E_1(N, S_{tot} = 0) - E_g(N) \tag{74}$$

$$\Delta E_{st} = E_0(N, S_{tot} = 1) - E_g(N) \tag{75}$$

The $E_0(N, S_{tot})$ and $E_1(N, S_{tot})$ are the lowest and the second lowest energies in the subspace with S_{tot} and $E_g = E_0(N, S_{tot} = 0)$.

From here the authors find that the critical point for this transition where these energies cross hence they sweep over J_1 and J_3 and set $J_2 = 1$ subspace to make the phase diagram. Which can be seen in figure 10.

From the phase diagram one is able to see that if either J_1 or J_3 is below 0.3 then the spin fluid phase (SF) is obtained. If $0.3 < J_1, J_3 < 1$ then we are in the dimer phase (D) and lastly if $J_1 > 1, J_3 > 1.0$ then we are in the ferrimagnetic phase.

The authors investigate the excitation energies of the dimer and the spin liquid phase by calculating the eigen energies with exact diagonalisation and the Lanczos algorithm. They have used spin systems sizes of 18 and 24, to investigate how the excitation spectres looks for for example the $\frac{1}{3}$ magnetization plateau. More information can be found in the article [16]

Kang et al. produced a model for the spins in azurite with six different exchange con-
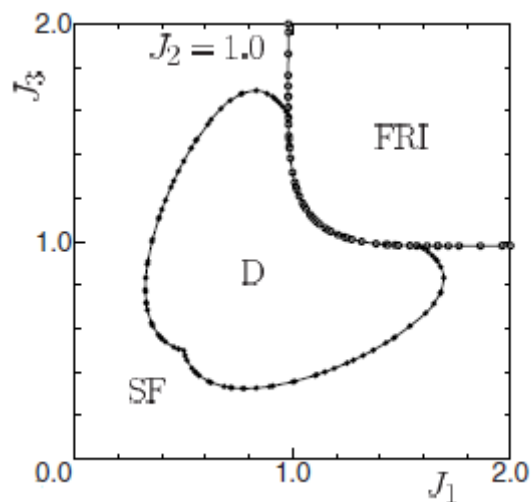

Figure 10: Phase diagram of the distorted diamond chain model [16] found by the method by [25].

stants seen in figure 11. This model is not only based on azurite but multiple diamond chain materials including $Na_2Cu_2TeO_6$ and $Bi_4Cu_3V_2O_{14}$ to name a few. The computational calculation method is called electronic structure calculations (which is good at identifying the leading exchange parameters of magnetic materials [12] [17]) [3].

By using Kikuchi[11][10][21] as stepping stones, using the Vienna *ab initio* simulation

package (VASP) [26] which uses generalized gradient approximations. They started the fitting analysis with the following exchange constants $\frac{J_2}{k_B} = 55$, $\frac{J_1}{k_B} = 1$, $\frac{J_3}{k_B} = -20$, $\frac{J_m}{k_B} = 10.1$, $\frac{J_d}{k_B} = 1.8$, these with the structural data they was able to conclude, that due to the electronic structure of azurite it should not be described as a diamond chain but as a 2D lattice where diamond chains are coupled through the exchange coupling of J_4. GGA stands for generalized gradient approximation, which is a approximation to the exchange correlation energy function in density functional theory (DFT) [19], and the U is the Cu $3d_{x^2-y^2}$ on cite Coulomb interaction strength. Their final exchange couplings are calculated with GGA+U where there are two different U, 4eV and 6eV. Both will be in the table underneath.

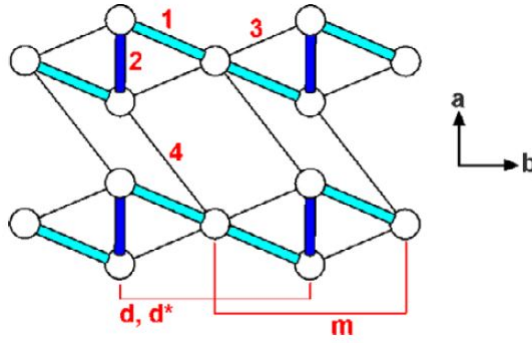The computational group Jeschke et. al.[7] worked with the density functional the-

Figure 11: Spin exchange paths of azurite shown with two diamond chains in the ab-plane, where the labels 1, 2, 3, 4, m, d and d refer to the spin exchange paths J_1, J_2, J_3, J_4, J_m and J_d, and J_{d*}, respectively. [9]

ory (DFT) calculations and the computational model based on different variants of the density-matrix renormalization group (DMRG) method and using the data from Kikuchi [11] [10]. From which they conclude that the dimer-monomer diamond chain model with the exchange constants J_1, J_2, J_3, J_m, are a good model to explain a broad range of experiments on azurite. Since the position of the lighter atoms (C, H, O) in azurite gained from experiments have a large error than the heavier atoms. They will start with a Car-Parrinello molecular dynamics calculation to determine positions of these to a unit cell of 30 atoms. With this structure they where able to gain the electronic properties which they uses with GGA+U calculations to find nine different exchange constants. First they analyses the interaction paths based on the GGA band structure, under the assumption that the exchange constants are antiferro magnetic. Then they use 2. order perturbation theory where $J_i^{AFM} = \frac{4t_i^2}{U}$. These constants can be found in

Jeschke et. al. [7] Table 1 and is called the full model. A minimal model which contain four exchange constants instead of the three in the other articles. Using the data from magnetization and INS experiments they was able to refine the exchange constants for a refined model of the minimal model. For the full models exchange constants, eight of these couplings are shown in figure 12 but it misses J_d which is the coupling of dimers. This coupling is parallel with J_m and couples two dimers together by coupling the "top" spins and the "bottom" spins to each other.

For the refined model $J_1 = 15.51K$, $J_2 = 33K$, $J_3 = 6.93K$ and $J_m = 4.62K$.The exchange constants of the refined model can be found in table 2. As seen in figure 13 Jeschke's computational data correspond very nicely with the magnetization curve that Kikuchi has measured[11][10], which will be described later.

Jeschke conclude that DFT calculations to fit the exchange constants with the data is not possible without guiding the four different exchange constants.
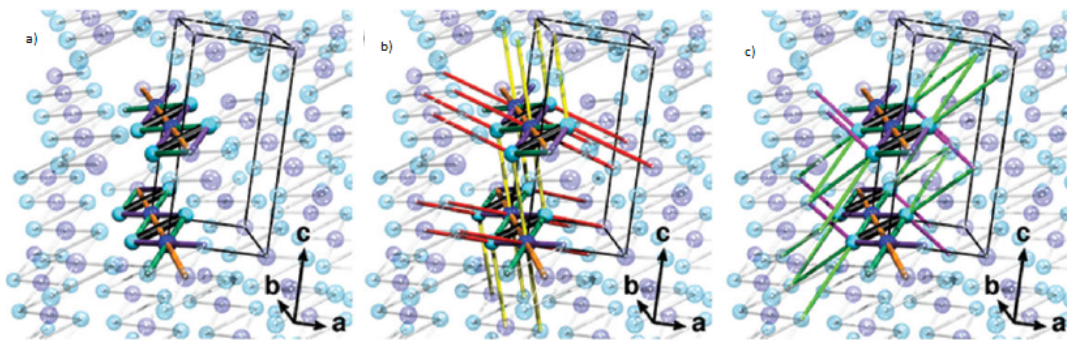

Figure 12: Arrangement of Cu_2 ions in the structure of azurite. The two inequivalent Cu_2 ions form dimers (cyan) and monomers (blue). (a) Most important exchange paths within the diamond chain running along the b axis: Dimer coupling J_2 (black), dimer-monomer couplings J_1 and J_3 (magenta and green), and monomer monomer coupling J_m (orange). (b)–(c) Three-dimensional couplings between diamond chains, connecting (b) monomer and dimer ions: J_5 (yellow) and J_6 (red) and (c) dimer ions only: J_4 (pink) and J_7 (light green).[7]

5.2 Exerimental studies

On the more experimental side, Kikuchi et. al.[10] [11], studied a natural single crystal of azurite. Powder X-ray diffraction was used to make sure the samples did not have impurities. Quantum Design PPMS was used to measure the susceptibility in the
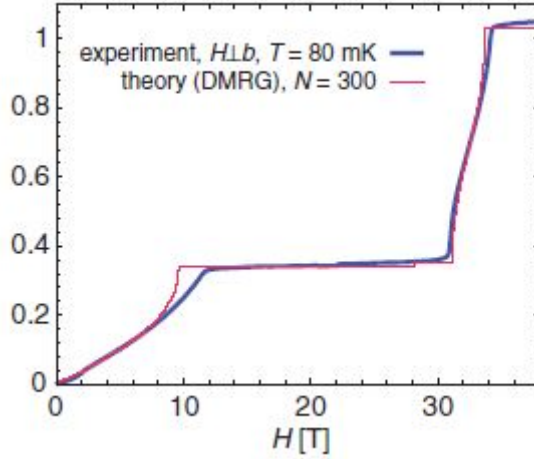
Figure 13: Comparison of computations for the magnetization curve found by DMRG for T = 0 and N = 300 spins with experimental data at T = 80 mK for H ⊥ b

temperature range between 2.0K - 300K with VSM and an applied external field of 0.1T. Induction method in a pulsed magnetic field was used to to measure the high field magnetization curves below 4.2K, and up to 60T. The specific heat was measured with the quasiadiabatic method from temperature $0.33K$ - $200K$. With a pulsed positive muon beam, the muon spin relaxation spectra was measured down to $0.02K$. H-NMR spectra and the spin-lattice relaxation time was measured at temperatures down to $1.7K$ and fields up to $15T$. [11].

They used an external perpendicular magnetic field from $0T$ - $60T$ and cooled the system all the way down to $80mK$. There is observed a spin-flip transition at $2.1T$ at $1.3K$ and $80mK$. But most interesting is the magnetization plateau that is clearly observed between $11.4T$ and $31T$. All this can be seen in figure 14.

By using the density matrix renormalization group method with the distorted diamond chain they was able to obtain a exchange constant ratio to represent the data, these are also shown in the figure 14 (b) as the dotted line.

There was a exact formula for H_s that was simplified to the case of isotropic diamond chain to be:

$$H_s = g\mu_B S(J_1 + J_3) \tag{76}$$

With this equation the exchange constants J_1 and J_3 has been found, to be $J_1 = 19K, J_2 = 24K$ $J_3 = 8.6K$, from calculations from $H_s = 33T$. These will also be shown in Table 2 From all these experiments I will use on the magnetization later in the thesis.
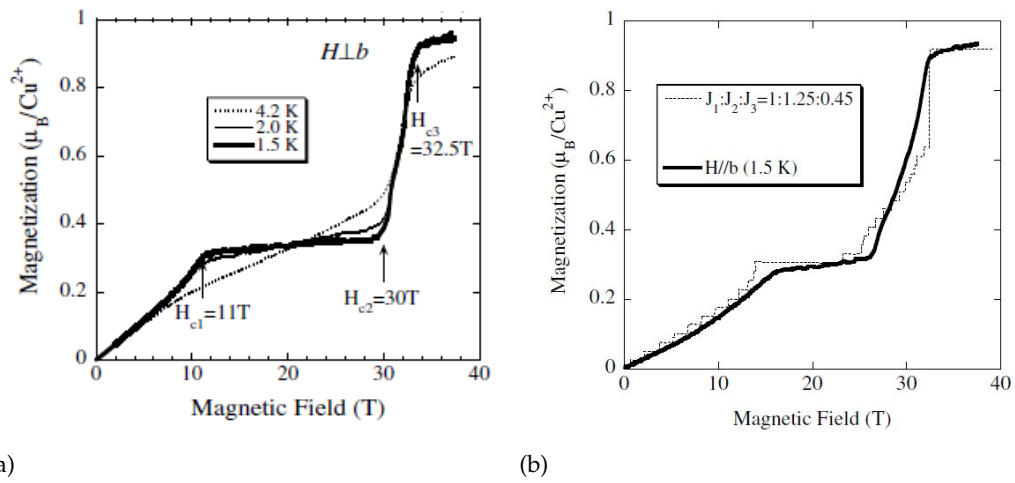
Figure 14: (
a)The high field magnetization curves of $Cu_3(CO_3)_2(OH)_2$ measured below 4.2 K. The magnetic field was applied perpendicular to the b axis (b) The best fitting result for the magnetization curve at 1.5 K for H ∥ b with the theoretical dotted line using $J_1:J_2:J_3=1:1.25:0.45$[10]
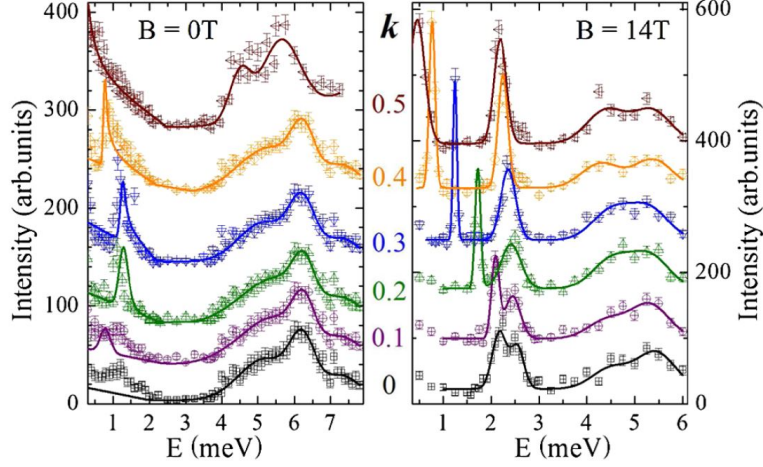
Figure 15: (color online). Energy dependence of the INS spectra of azurite at $\mathbf{q} = (1, k, 0)$, $k = 0$ to 0.5, in zero field (left) and a field of 14T $\perp b^*$ (right) at $T = 1.5$K. Lines indicate fits to the data, which are shifted due to clarity

Other experiments on azurite was performed by the group of Rule et. al. [21][23][22]. Rule starts to study azurite with specific heat and inelastic neutron scattering (INS) measurements. They have used a naturally grown azurite crystal for both of the two different experiment types. From the crystal 0.36 g was cut off to do the specific heat measurements ($C_p(T)$), which was measured in the temperature range of 1.6 to 30K on an ac-calorimeter. They have an external field pointing at the *ac*-plane and 65° away from the c-axis, why this direction is because they approximate that this is the easiest axis of the AFM phase below $T = 1.85$K.

To start the analysis of the experiment they uses the Dimer-monomer model, which has the inter-dimer exchange constant J_2 that is the dominating the other exchange constants (J_1, J_3) on the energy scale.

The INS was to gain magnetic excitation both at 0 T and 14 T field measured at $T = 1.5$K to avoid thermal line broadening and adverse effects from structural distortion, which have been observed at 1.86K. The data fits in figure 15 was produced by combining Gaussian line shapes above 2 meV and calculated using a 1D chain convoluted with instrumental resolution and the copper form factor for below 2 meV. By fitting the Gaussian to the peak positions in multiple different plot(see in article [21]) they gain different expressions of the energy and with these expressions they come up with the following coupling constants, $J_1 \simeq 1$K, $J_3 \simeq -20$K, $J_2 = 55$K, $J_{mono} = 10.1$K, $J_{dimer} = 1.8$K.

The next experiment Rule[23] performed a INS, below the magnetization plateau at

$B = 11T$. With the considerations that the symmetry of azurite was $P2_1$ and the magnetic moment was found to be two different, one for the dimer ($m_0 = 0.684\mu_B$ and one for monomer ($m_0 = 0.264\mu_B$ [23]. They compared the data with the ideal Heisenberg model and to find inconsistencies.

These calculations was performed with the ABACUS algorithm, which is a algorithm to calculate the dynamical correlation functions of some important observable of the system such as Heisenberg spin chain[2], and with the anisotropic Heisenberg Hamiltonian:

$$H = \sum_{j=1}^{N} J_x S_j^x S_{j+1}^x + J_y S_j^y S_{j+1}^y + J_z S_j^z S_{j+1}^z - H_z S_j^z \qquad (77)$$

where H_z is the applied field and are increasing up to observe the plateau limit $H_z \approx$ 11.T H_z are coupled to relative values of J_x, J_y and J_z.

With these data and calculations they were able to conclude that azurite is not well described by the 1D Heisenberg chain.

5.3   Other materials

The last article to be mentioned in this composition of articles are Honecker and Läuchli [4] who does calculations on another material ($Cu_3Cl_6(H_2O)_2\cdot 2H_8C_4SO_2$). The model to describe this material is also the diamond chain with three exchange constants. This article takes a theoretical approach to find a suitable spin model to and compares with data of susceptibility and specific heat[4]. They uses the Heisenberg Hamiltonian from eq 72. From fitting the result from the Lanczos exact energies to the susceptibility data they found that at least one of J_1 or J_3 should be ferromagnetic. They came to the conclusion that the data compared the best when $J_1 = -260 \pm 50K$, $J_2 = 250 \pm 40K$ and $J_3 = -40 \pm 30K$. With these values they could find the $\frac{1}{3}$- magnetization plateau which is shown in figure 16, since the material is not azurite. The plateau is placed differently than for azurite as a function of applied field.

In this thesis I will use RLexact to produce magnetisation data with all the exchange couplings constants given from the articles are inserted in table 2.
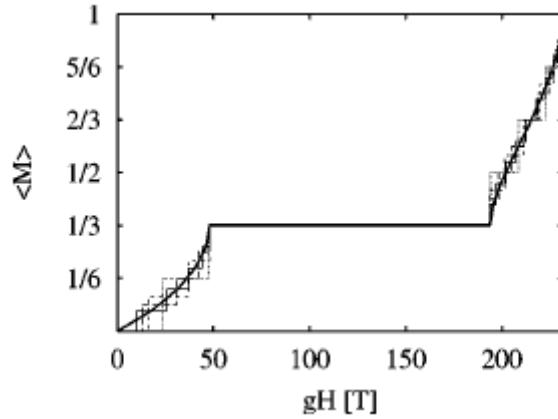
Figure 16: Magnetization curve for $J_1 = -300K$, $J_2 = 280K$, and $J_3 = -60K$. Which is multiplied with $g = 2.03$. The thick line is an extrapolation whereas thin lines are for finite system sizes: $L = 12$(dotted), $L = 18$(short dashes), $L = 24$ (long dashes), and $L = 30$ (full)[4]

	J_1	J_2	J_3	J_4	J_d	J_m
Kang U = 4 eV [9]	89.4	363.3	86.1	46.3	-6.7	0.1
Kang U = 6 eV [9]	52.6	221.7	46.3	27.4	0.15	1.2
Jeschke refined [7]	15.51	33	6.43	0	0	4.62
Kikuchi [11]	19	24	8.6	0	0	0
Rule [21]	1	55	-20	0	1.8	10.1

Table 2: Collected exchange constants for azurite, taken from literature, all in units of K

6 Code Validation

6.1 Current state of RLexact

When I started this thesis RLexact was able to calculate energies, correlation functions $S^{zz}(\mathbf{q}, \omega)$, $S^{xx}(\mathbf{q}, \omega)$, $S^{yy}(\mathbf{q}, \omega)$, $S^{+-}(\mathbf{q}, \omega)$ and $S^{-+}(\mathbf{q}, \omega)$ for the transveres Ising model and for 1D, 2D and 3D magnetic systems without any applied magnetic field. Symmetries included are the translational symmetry, mirror symmetry and the total S^z symmetry (in RLexact its called m-symmetry). No improvements to RLexact has been done in this thesis.

6.2 Validation

To validate RLexacts calculations, I have used the diamond chain model from azurite and made a system of 6 spins with five different J's as the articles propose. These calculations will then be compared with the calculations of RLexact. Due to there being no mirror symmetry in the 1D diamond chain (Azurite), this part has been cut out.

To start I have taken all positive M's and in this case this will be M = 0, 1, 2 and 3. Every single possible way of the system has then been categorized as for M = 2 $|0\rangle = |\downarrow\uparrow\uparrow\uparrow\uparrow\uparrow\rangle$, following is shown below. The translational symmetry is used on these states to show its effect.

$$|0\rangle = |\downarrow\uparrow\uparrow\uparrow\uparrow\uparrow\rangle \qquad |1\rangle = |\uparrow\downarrow\uparrow\uparrow\uparrow\uparrow\rangle \qquad |2\rangle = |\uparrow\uparrow\downarrow\uparrow\uparrow\uparrow\rangle$$

$$|3\rangle = |\uparrow\uparrow\uparrow\downarrow\uparrow\uparrow\rangle \qquad |4\rangle = |\uparrow\uparrow\uparrow\uparrow\downarrow\uparrow\rangle \qquad |5\rangle = |\uparrow\uparrow\uparrow\uparrow\uparrow\downarrow\rangle$$

$$\hat{T}|0\rangle = |3\rangle \qquad\qquad \hat{T}|1\rangle = |4\rangle \qquad\qquad \hat{T}|2\rangle = |5\rangle$$

Hereafter, the states that are able to become each other with the use of translational symmetry will be set into "groups". Such as $|M, t, j\rangle$ where M is the magnetisation, t is the translation symmetry and j is the different configurations.

$H|2;0,0\rangle = (|0\rangle + |3\rangle) * \frac{1}{\sqrt{2}}$
$H|2;0,1\rangle = (|1\rangle + |4\rangle) * \frac{1}{\sqrt{2}}$
$H|2;0,2\rangle = (|2\rangle + |5\rangle) * \frac{1}{\sqrt{2}}$

$H|2;1,0\rangle = (|0\rangle - |3\rangle) * \frac{1}{\sqrt{2}}$
$H|2;1,1\rangle = (|1\rangle - |4\rangle) * \frac{1}{\sqrt{2}}$
$H|2;1,2\rangle = (|2\rangle - |5\rangle) * \frac{1}{\sqrt{2}}$

From these it is possible to combine some of them into small matrices, as shown below. It is also possible to set them into a big matrix but since they will have no interactions between each of the small ones (and the big will not be able to be on one page, therefore will i keep the small).

	$\lvert 2;0,0\rangle$	$\lvert 2,0,1\rangle$	$\lvert 2;0,2\rangle$
$\lvert 2,0,0\rangle$	$\frac{J_2}{2} + \frac{J_m}{2} + J_d$	$\frac{J_1}{2} + \frac{J_3}{2}$	$\frac{J_1}{2} + \frac{J_3}{2}$
$\lvert 2,0,1\rangle$	$\frac{J_1}{2} + \frac{J_3}{2}$	$\frac{J_1}{2} + \frac{J_3}{2} + \frac{J_m}{2} + J_d$	$\frac{J_2}{2}$
$\lvert 2;0,2\rangle$	$\frac{J_1}{2} + \frac{J_3}{2}$	$\frac{J_2}{2}$	$\frac{J_1}{2} + \frac{J_3}{2} + \frac{J_m}{2} + J_d$

Table 3: Hamiltonian on matrix form of $\lvert 2;0,0\rangle$, $\lvert 2;0,1\rangle$ and $\lvert 2;0,2\rangle$.

	$\lvert 2;1,0\rangle$	$\lvert 2,1,1\rangle$	$\lvert 2;1,2\rangle$
$\lvert 2,1,0\rangle$	$\frac{J_2}{2} - \frac{3*J_m}{2} + J_d$	$-\frac{J_1}{2} + \frac{J_3}{2}$	$\frac{J_1}{2} - \frac{J_3}{2}$
$\lvert 2,1,1\rangle$	$-\frac{J_1}{2} + \frac{J_3}{2}$	$\frac{J_1}{2} + \frac{J_3}{2} + \frac{J_m}{2} - J_d$	$\frac{J_2}{2}$
$\lvert 2;1,2\rangle$	$\frac{J_1}{2} - \frac{J_3}{2}$	$\frac{J_2}{2}$	$\frac{J_1}{2} + \frac{J_3}{2} + \frac{J_m}{2} - J_d$

Table 4: Hamiltonian on matrix form of $\lvert 2;1,0\rangle$, $\lvert 2;1,1\rangle$ and $\lvert 2;1,2\rangle$.

These matrices can then be diagonalized and the result will then be collected and inserted in the following table. To make sure the calculations by RLexact are correct then one of the five different J's will have the strength of 1 while the other has the strength of 0.01 to make sure no shenanigans happens, this will be done for all of them.

As seen in the table the analytical calculations do agree with the calculations done by RLexact.

	$\lvert 1,0,0\rangle$	$\lvert 1,0,1\rangle$	$\lvert 1,0,2\rangle$	$\lvert 1,0,3\rangle$	$\lvert 1,0,4\rangle$	$\lvert 1,0,5\rangle$	$\lvert 1,0,6\rangle$	$\lvert 1,0,7\rangle$	$\lvert 1,0,8\rangle$
$\lvert 1,0,0\rangle$	$-J_1+\frac{J_2}{2}-J_3+\frac{J_m}{2}+J_d$	0	$\frac{J_1}{\sqrt{2}}$	$\frac{J_3}{\sqrt{2}}$	0	$\frac{J_3}{\sqrt{2}}$	$\frac{J_1}{\sqrt{2}}$	0	0
$\lvert 1,0,1\rangle$	0	$\frac{J_2}{2}+\frac{J_m}{2}-J_d$	$\frac{J_3}{2}$	$2\cdot J_d$	$\frac{J_3}{2}$	$\frac{J_1}{2}$	0	0	0
$\lvert 1,0,2\rangle$	$\frac{J_1}{\sqrt{2}}$	$\frac{J_3}{2}$	$-\frac{J_1}{2}-\frac{J_m}{2}+\frac{J_3}{2}$	$\frac{J_2}{2}$	$\frac{J_3}{2}$	J_d+J_m	0	$\frac{J_1}{\sqrt{2}}$	0
$\lvert 1,0,3\rangle$	$\frac{J_3}{\sqrt{2}}$	$2\cdot J_d$	$\frac{J_2}{2}$	$\frac{J_1}{2}-\frac{J_3}{2}-\frac{J_m}{2}$	$\frac{J_1}{2}$	0	J_d+J_m	0	$\frac{J_3}{\sqrt{2}}$
$\lvert 1,0,4\rangle$	0	$\frac{J_3}{2}$	$\frac{J_3}{2}$	$\frac{J_1}{2}$	$-\frac{J_2}{2}+\frac{J_m}{2}-J_d$	$\frac{J_1}{2}$	0	$\frac{J_2}{\sqrt{2}}$	$\frac{J_2}{\sqrt{2}}$
$\lvert 1,0,5\rangle$	$\frac{J_3}{\sqrt{2}}$	$\frac{J_1}{2}$	J_d+J_m	0	$\frac{J_1}{2}$	$-\frac{J_m}{2}+\frac{J_1}{2}-\frac{J_3}{2}$	$\frac{J_2}{2}$	$\frac{J_3}{\sqrt{2}}$	0
$\lvert 1,0,6\rangle$	$\frac{J_1}{\sqrt{2}}$	0	0	J_d+J_m	0	$\frac{J_2}{2}$	$-\frac{J_m}{2}-\frac{J_1}{2}+\frac{J_3}{2}$	0	$\frac{J_1}{\sqrt{2}}$
$\lvert 1,0,7\rangle$	0	0	$\frac{J_1}{\sqrt{2}}$	0	$\frac{J_2}{\sqrt{2}}$	$\frac{J_3}{\sqrt{2}}$	0	$-\frac{J_2}{2}+\frac{J_m}{2}+J_d$	0
$\lvert 1,0,8\rangle$	0	0	0	$\frac{J_3}{\sqrt{2}}$	$\frac{J_2}{\sqrt{2}}$	0	$\frac{J_1}{\sqrt{2}}$	0	$-\frac{J_2}{2}+\frac{J_m}{2}+J_d$

Table 5: Hamiltonian on matrix form of $\lvert 1;0,0\rangle$, $\lvert 1;0,1\rangle$, $\lvert 1;0,2\rangle$, $\lvert 1;0,3\rangle$, $\lvert 1;0,4\rangle$, $\lvert 1;0,5\rangle$, $\lvert 1;0,6\rangle$, $\lvert 1;0,7\rangle$ and $\lvert 1;0,8\rangle$.

	$\lvert 1,1,1\rangle$	$\lvert 1,1,2\rangle$	$\lvert 1,1,3\rangle$	$\lvert 1,1,4\rangle$	$\lvert 1,1,5\rangle$	$\lvert 1,1,6\rangle$
$\lvert 1,1,1\rangle$	$\frac{J_2}{2} + \frac{J_m}{2} - J_d$	$\frac{J_1}{2}$	$\frac{J_3}{2}$	0	$-\frac{J_3}{2}$	$-\frac{J_1}{2}$
$\lvert 1,1,2\rangle$	$\frac{J_1}{2}$	$-\frac{J_1}{2} + \frac{J_3}{2} - \frac{J_m}{2}$	$\frac{J_2}{2}$	$-\frac{J_3}{2}$	$J_d - J_m$	0
$\lvert 1,1,3\rangle$	$\frac{J_3}{2}$	$\frac{J_2}{2}$	$\frac{J_1}{2} - \frac{J_3}{2} - \frac{J_m}{2}$	$\frac{J_1}{2}$	0	$J_d - J_m$
$\lvert 1,1,4\rangle$	0	$-\frac{J_3}{2}$	$\frac{J_1}{2}$	$-\frac{J_2}{2} + \frac{J_m}{2} - J_d$	$\frac{J_1}{2}$	$-\frac{J_3}{2}$
$\lvert 1,1,5\rangle$	$-\frac{J_3}{2}$	$J_d - J_m$	0	$\frac{J_1}{2}$	$\frac{J_1}{2} - \frac{J_3}{2} - \frac{J_m}{2}$	$\frac{J_2}{2}$
$\lvert 1,1,6\rangle$	$-\frac{J_1}{2}$	0	$J_d - J_m$	$-\frac{J_3}{2}$	$\frac{J_2}{2}$	$-\frac{J_1}{2} + \frac{J_3}{2} - \frac{J_m}{2}$

Table 6: Hamiltonian on matrix form of $\lvert 1;1,1\rangle$, $\lvert 1;1,2\rangle$, $\lvert 1;1,3\rangle$, $\lvert 1;1,4\rangle$, $\lvert 1;1,5\rangle$, and $\lvert 1;1,6\rangle$.

Table 7 (rotated landscape). Hamiltonian matrix in the basis $|0,0,0\rangle,\ldots,|0,0,9\rangle$.

	$|0,0,0\rangle$	$|0,0,1\rangle$	$|0,0,2\rangle$	$|0,0,3\rangle$	$|0,0,4\rangle$	$|0,0,5\rangle$	$|0,0,6\rangle$	$|0,0,7\rangle$	$|0,0,8\rangle$	$|0,0,9\rangle$
$|0,0,0\rangle$	$\frac{I_2}{2}-I_m/2-I_d$	$\frac{I_1}{2}$	0	I_d	$\frac{I_3}{2}$	I_d	I_m	$\frac{I_3}{2}$	$\frac{I_3}{2}$	$\frac{I_1}{2}$
$|0,0,1\rangle$	$\frac{I_1}{2}$	$-\frac{I_1}{2}-\frac{I_3}{2}+I_m/2+I_d$	$\frac{I_1}{2}+\frac{I_3}{2}$	$\frac{I_3}{2}$	$\frac{I_2}{2}$	$\frac{I_1}{2}$	$\frac{I_2}{2}$	$\frac{I_3}{2}$	$\frac{I_3}{2}$	0
$|0,0,2\rangle$	0	$\frac{I_1}{2}+\frac{I_3}{2}$	$-\frac{I_2}{2}-\frac{I_m}{2}+I_d+I_m$	$\frac{I_2}{2}$	0	$\frac{I_2}{2}$	0	0	$\frac{I_1}{2}+\frac{I_3}{2}$	0
$|0,0,3\rangle$	$\frac{I_d}{2}$	$\frac{I_3}{2}$	$\frac{I_2}{2}$	$I_1-\frac{I_2}{2}-I_3-I_m/2-I_d$	$\frac{I_1}{2}+\frac{I_3}{2}$	$\frac{I_2}{2}$	$\frac{I_d}{2}$	$\frac{I_3}{2}$	$\frac{I_3}{2}$	$\frac{I_2}{2}$
$|0,0,4\rangle$	I_d	$\frac{I_2}{2}$	0	$\frac{I_1}{2}+\frac{I_3}{2}$	$-\frac{I_1}{2}-\frac{I_3}{2}+I_m/2+I_d$	$\frac{I_m}{2}$	$\frac{I_2}{2}$	$\frac{I_1}{2}$	$\frac{I_1}{2}$	$\frac{I_3}{2}$
$|0,0,5\rangle$	0	$\frac{I_2}{2}$	$\frac{I_2}{2}$	$\frac{I_m}{2}$	$\frac{I_1}{2}$	$I_1-\frac{I_2}{2}-I_3-I_m/2-I_d+I_d$	$\frac{I_2}{2}$	I_d	$\frac{I_1}{2}$	$\frac{I_2}{2}$
$|0,0,6\rangle$	I_m	$\frac{I_3}{2}$	0	$\frac{I_d}{2}$	$\frac{I_2}{2}$	$\frac{I_2}{2}$	$-\frac{I_2}{2}-I_m/2+I_d+I_m$	0	0	$\frac{I_1}{2}+\frac{I_3}{2}$
$|0,0,7\rangle$	$\frac{I_3}{2}$	0	0	$\frac{I_3}{2}$	$\frac{I_1}{2}$	I_d	0	$\frac{I_2}{2}-I_m/2-I_d$	$\frac{I_1}{2}$	$\frac{I_2}{2}$
$|0,0,8\rangle$	$\frac{I_3}{2}$	0	$\frac{I_1}{2}+\frac{I_3}{2}$	$\frac{I_3}{2}$	$\frac{I_1}{2}$	$\frac{I_1}{2}$	0	$\frac{I_1}{2}$	$-I_1-\frac{I_3}{2}-\frac{I_2}{2}+I_m/2+I_d$	$\frac{I_2}{2}$
$|0,0,9\rangle$	$\frac{I_1}{2}$	0	0	$\frac{I_2}{2}$	$\frac{I_3}{2}$	$\frac{I_2}{2}$	$\frac{I_1}{2}+\frac{I_3}{2}$	$\frac{I_2}{2}$	$\frac{I_2}{2}$	$-\frac{I_2}{2}-\frac{I_3}{2}+I_m/2+I_d$

Table 7: Hamiltonian on matrix form of $|0,0,0\rangle$, $|0,0,1\rangle$, $|0,0,2\rangle$, $|0,0,3\rangle$, $|0,0,4\rangle$, $|0,0,5\rangle$, $|0,0,6\rangle$, $|0,0,7\rangle$, $|0,0,8\rangle$ and $|0,0,9\rangle$.

	$|0,1,0\rangle$	$|0,1,1\rangle$	$|0,1,2\rangle$	$|0,1,3\rangle$	$|0,1,4\rangle$	$|0,1,5\rangle$	$|0,1,6\rangle$	$|0,1,7\rangle$	$|0,1,8\rangle$	$|0,1,9\rangle$
$|0,1,0\rangle$	$\frac{J_2}{2}-J_m/2-J_d$	$\frac{J_1}{2}$	0	J_d	0	J_d	0	$-J_m$	0	$-\frac{J_1}{2}$
$|0,1,1\rangle$	$\frac{J_1}{2}$	$-\frac{J_1}{2}-\frac{J_3}{2}+J_m/2-J_d$	$\frac{J_1}{2}-\frac{J_3}{2}$	$\frac{J_3}{2}$	$\frac{J_2}{2}$	$-\frac{J_1}{2}$	0	$-\frac{J_3}{2}$	0	0
$|0,1,2\rangle$	0	$\frac{J_1}{2}-\frac{J_3}{2}$	$-\frac{J_2}{2}-J_m/2+J_d-J_m$	$\frac{J_2}{2}$	0	$\frac{J_2}{2}$	0	0	$-\frac{J_1}{2}+\frac{J_3}{2}$	0
$|0,1,3\rangle$	J_d	$\frac{J_3}{2}$	$\frac{J_2}{2}$	$J_1-\frac{J_2}{2}-J_3-J_m/2-J_d$	$-\frac{J_3}{2}$	$\frac{J_2}{2}$	J_d	$J_d-\frac{J_1}{2}$	$-\frac{J_3}{2}$	$-\frac{J_3}{2}$
$|0,1,4\rangle$	0	$\frac{J_2}{2}$	0	$-\frac{J_3}{2}$	$-\frac{J_1}{2}-\frac{J_3}{2}+J_m/2-J_d$	$-\frac{J_1}{2}$	$-\frac{J_1}{2}$	J_d	0	0
$|0,1,5\rangle$	J_d	$-\frac{J_1}{2}$	$\frac{J_2}{2}$	$\frac{J_2}{2}$	$-\frac{J_1}{2}$	$J_1-\frac{J_2}{2}-J_3-J_m/2-J_d-J_d$	$\frac{J_2}{2}$	$\frac{J_2}{2}$	$-\frac{J_1}{2}$	$-\frac{J_1}{2}$
$|0,1,6\rangle$	0	0	0	J_d	$-\frac{J_1}{2}$	$\frac{J_2}{2}$	$-\frac{J_2}{2}-J_m/2+J_d-J_m$	0	$-\frac{J_1}{2}$	$-\frac{J_1}{2}$
$|0,1,7\rangle$	$-J_m$	$-\frac{J_3}{2}$	0	$J_d-\frac{J_1}{2}$	J_d	$\frac{J_2}{2}$	0	$\frac{J_2}{2}-J_m/2-J_d$	$-\frac{J_3}{2}$	$-\frac{J_3}{2}$
$|0,1,8\rangle$	0	0	$-\frac{J_1}{2}+\frac{J_3}{2}$	$-\frac{J_3}{2}$	0	$-\frac{J_1}{2}$	$-\frac{J_1}{2}$	$-\frac{J_3}{2}$	$-\frac{J_1}{2}-\frac{J_3}{2}+J_m/2-J_d$	$-\frac{J_1}{2}$
$|0,1,9\rangle$	$-\frac{J_1}{2}$	0	0	$-\frac{J_3}{2}$	0	$-\frac{J_1}{2}$	$-\frac{J_1}{2}$	$-\frac{J_3}{2}$	$-\frac{J_1}{2}$	$-\frac{J_1}{2}-\frac{J_3}{2}+J_m/2-J_d$

Table 8: Hamiltonian on matrix form of $|0,1,0\rangle$, $|0,1,1\rangle$, $|0,1,2\rangle$, $|0,1,3\rangle$, $|0,1,4\rangle$, $|0,1,5\rangle$, $|0,1,6\rangle$, $|0,1,7\rangle$, $|0,1,8\rangle$ and $|0,1,9\rangle$.

M	State	Analytical Energies
3	$\lvert 3;0,0\rangle$	$J_1 + \frac{J_2}{2} + J_3 + \frac{J_m}{2} + J_d$
2	$-2\cdot\lvert 2;0,0\rangle + \lvert 2;0,1\rangle + \lvert 2;0,2\rangle$	$\frac{J_1}{2} - \frac{J_2}{2} + \frac{J_3}{2} + \frac{J_m}{2} + J_d$
2	$-\lvert 2;0,1\rangle + \lvert 2;0,2\rangle$	$-\frac{J_1}{2} - \frac{J_2}{2} - \frac{J_3}{2} + \frac{J_m}{2} + J_d$
2	$\lvert 2;0,0\rangle + \lvert 2;0,1\rangle + \lvert 2;0,2\rangle$	$J_1 + \frac{J_2}{2} + J_3 + \frac{J_m}{2} + J_d$
2	$-2\cdot\lvert 2;1,0\rangle - \lvert 2;1,1\rangle + \lvert 2;1,2\rangle$	$\frac{J_1}{2} + \frac{J_2}{2} + \frac{J_3}{2} + \frac{J_m}{2} - J_d$
2	$\lvert 2;1,1\rangle + \lvert 2;1,2\rangle$	$\frac{J_1}{4} + \frac{J_3}{4} - \frac{J_m}{2} - \frac{\sqrt{9\cdot J_1^2 - 4\cdot J_1\cdot J_2 - 14\cdot J_1\cdot J_3 - 8\cdot J_1\cdot J_d + 8\cdot J_1\cdot J_m + 4\cdot J_2^2 - 4\cdot J_2\cdot J_3 + 16\cdot J_2\cdot J_d - 16\cdot J_2\cdot J_m + 9\cdot J_3^2 - 8\cdot J_3\cdot J_d + 8\cdot J_3\cdot J_m + 16\cdot J_d^2 - 32\cdot J_d\cdot J_m + 16\cdot J_m^2}}{4}$
2	$\lvert 2;1,0\rangle - \lvert 2;1,1\rangle + \lvert 2;1,2\rangle$	$J_1\cdot 2 + \frac{J_2}{2}$
1	$\lvert 1;1,1\rangle - \lvert 1;1,2\rangle + \lvert 1;1,6\rangle$	$\frac{J_1}{2} + \frac{J_2}{2} + \frac{J_3}{2} - J_d + \frac{J_m}{2}$
1	$\lvert 1;1,2\rangle - \lvert 1;1,3\rangle + 2\cdot\lvert 1;1,4\rangle - \lvert 1;1,5\rangle + \lvert 1;1,6\rangle$	$-\frac{J_1}{2} - \frac{J_2}{2} - \frac{J_3}{2} - J_d + \frac{J_m}{2}$
1	$\lvert 1;1,2\rangle + \frac{1}{3}\cdot\lvert 1;1,3\rangle - \frac{2}{3}\cdot\lvert 1;1,4\rangle + \frac{1}{3}\cdot\lvert 1;1,5\rangle + \lvert 1;1,6\rangle$	$-\frac{J_1}{4} - \frac{J_3}{4} - \frac{J_m}{2} - \frac{\sqrt{9\cdot J_1^2 - 4\cdot J_1\cdot J_2 - 14\cdot J_1\cdot J_3 + 8\cdot J_1\cdot J_d - 8\cdot J_1\cdot J_m + 4\cdot J_2^2 - 4\cdot J_2\cdot J_3 - 16\cdot J_2\cdot J_d + 16\cdot J_2\cdot J_m + 9\cdot J_3^2 + 8\cdot J_3\cdot J_d - 8\cdot J_3\cdot J_m + 16\cdot J_d^2 - 32\cdot J_d\cdot J_m + 16\cdot J_m^2}}{4}$
1	$-2\cdot\lvert 1;1,1\rangle - \lvert 1;1,2\rangle + 3\cdot\lvert 1;1,3\rangle - 3\cdot\lvert 1;1,5\rangle + \lvert 1;1,6\rangle$	$-\frac{J_1}{4} - \frac{J_3}{4} - \frac{J_m}{2} + \frac{sqrt 9\cdot J_1^2 - 4\cdot J_1\cdot J_2 - 14\cdot J_1\cdot J_3 + 8\cdot J_1\cdot J_d - 8\cdot J_1\cdot J_m + 4\cdot J_2^2 - 4\cdot J_2\cdot J_3 - 16\cdot J_2\cdot J_d + 16\cdot J_2\cdot J_m + 9\cdot J_3^2 + 8\cdot J_3\cdot J_d - 8\cdot J_3\cdot J_m + 16\cdot J_d^2 - 32\cdot J_d\cdot J_m + 16\cdot J_m^2}{4}$
1	$-2\cdot\lvert 1;1,1\rangle - \lvert 1;1,2\rangle - \lvert 1;1,3\rangle + \lvert 1;1,5\rangle + \lvert 1;1,6\rangle$	$\frac{J_1}{4} + \frac{J_3}{4} - \frac{J_m}{2} - \frac{\sqrt{9\cdot J_1^2 - 4\cdot J_1\cdot J_2 - 14\cdot J_1\cdot J_3 - 8\cdot J_1\cdot J_d + 8\cdot J_1\cdot J_m + 4\cdot J_2^2 - 4\cdot J_2\cdot J_3 + 16\cdot J_2\cdot J_d - 16\cdot J_2\cdot J_m + 9\cdot J_3^2 - 8\cdot J_3\cdot J_d + 8\cdot J_3\cdot J_m + 16\cdot J_d^2 - 32\cdot J_d\cdot J_m + 16\cdot J_m^2}}{4}$
1	$\lvert 1;1,3\rangle + \lvert 1;1,4\rangle + \lvert 1;1,5\rangle$	$\frac{J_1}{4} + \frac{J_3}{4} - \frac{J_m}{2} + \frac{\sqrt{9\cdot J_1^2 - 4\cdot J_1\cdot J_2 - 14\cdot J_1\cdot J_3 - 8\cdot J_1\cdot J_d + 8\cdot J_1\cdot J_m + 4\cdot J_2^2 - 4\cdot J_2\cdot J_3 + 16\cdot J_2\cdot J_d - 16\cdot J_2\cdot J_m + 9\cdot J_3^2 - 8\cdot J_3\cdot J_d + 8\cdot J_3\cdot J_m + 16\cdot J_d^2 - 32\cdot J_d\cdot J_m + 16\cdot J_m^2}}{4}$

Table 9: Analytical results obtained for the 13 energies (missing $\lvert 1,0,j\rangle$, $\lvert 0,0,j\rangle$ and $\lvert 0,1,j\rangle$ since the matrices becomes 9x9 and 10x10 and was hard to do analytic by hand) in the case N=6 spins, as a function of the five coupling constants J_1, J_2, J_3, J_m, J_d. J_1 is $J_1 = 1, J_2 = 0.01, J_3 = 0.01, J_m = 0.01, J_d = 0.01$ and J_2 is $J_1 = 0.01, J_2 = 1, J_3 = 0.01, J_m = 0.01, J_d = 0.01$ and so forth.

| M	Hand J_1	RLexact J_1	Hand J_2	RLexact J_2	Hand J_3	RLexact J_3	Hand J_m	RLexact J_m	Hand J_d	RLexact J_d
3	1.03	1.03	0.535	0.535	1.03	1.03	0.535	0.535	1.03	1.03
2	-0.485	-0.485	0.505	0.505	-0.485	-0485	0.505	0.505	1.0	1.0
2	0.515	0.515	-0.475	-0.475	0.515	0.515	0.515	0.515	1.01	1.01
2	1.03	1.03	0.535	0.535	1.03	1.03	0.535	0.535	1.03	1.03
2	-0.495	-0.495	-0.495	-0.495	-0.495	-0.495	-1.485	-1.485	-0.99	-0.99
2	0.505	0.505	0.505	0.505	0.505	0.505	0.505	0.505	-0.98	-0.98
2	0.99	0.99	0.495	0.495	0.99	0.99	0.495	0.495	0.99	0.99
1	-1.0	-1.0	-0.505	-0.505	-1.0	-1.0	-1.495	-1.495	-1.0	-1.0
1	0.505	0.505	0.505	0.505	0.505	0.505	0.505	0.505	-0.98	-0.98
1	0.485	0.485	0.485	0.485	0.485	0.485	0.485	0.485	0.98	0.98
1	0.99	0.99	0.495	0.495	0.99	0.99	0.495	0.495	0.99	0.99
1	-0.495	-0.495	-0.495	-0.495	-0.495	-0.495	-1.485	-1.485	-0.99	-0.99
1	-0.515	-0.515	-0.515	-0.515	-0.515	-0.515	0.475	0.475	-1.01	-1.01

Table 10: Numerical results obtained for the 13 energies above in the case N=6 spins, as a function of the five coupling constants J_1, J_2, J_3, J_m, J_d. J_1 is $J_1 = 1, J_2 = 0.01, J_3 = 0.01, J_m = 0.01, J_d = 0.01$ and J_2 is $J_1 = 0.01, J_2 = 1, J_3 = 0.01, J_m = 0.01, J_d = 0.01$ and so forth.
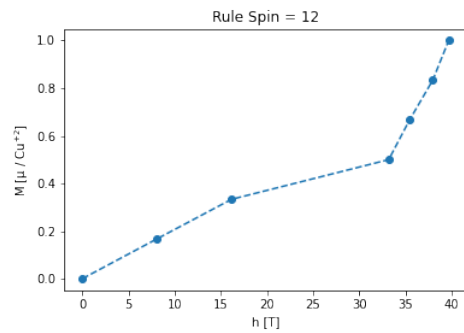
7 Results

RLexact returns energies corresponding to a given *M*- and *q*-value. These energies are then subtracted from the ground state energy and plotted up vs the q's for the excitation plots. Each article will be compared to my results with their interaction constants in discussion. The interactions constats used fore these Rlexact calculations are found in table 2.

7.1 Scaling

RLexact calculations for spin system sizes of 6, 12, 18, 24 and 30 spins are shown in figure 17 (a-e). All of them have a plateau at $\frac{1}{3}$ magnetization (exapt it is hard to see on the 6 spin system plot). The higher we go in the system size the more "flat" the plateau will seem. This is due to the fact that there wwill be more allowed values of the magnetization when the system size is increased. So the plots will become more "compressed". The system sizes that look most like the data from the article (lets use Rule as an example), is seen in figure 17 (f), of system size 24 and 30 spin. These two system sizes will be used in further investigation of the data in magnetization and excitation plots. For excitation scaling, the data will gain energies for higher q-values for larger systems. For the 6 spin system the excitation energies will have q-values of 0 and 1, corresponding to 0 and π in r.l.u. for 30 spins they will have q-values of 0-9. This will give a higher resolution and it will therefore be easier to see the dispersion of the spin waves.
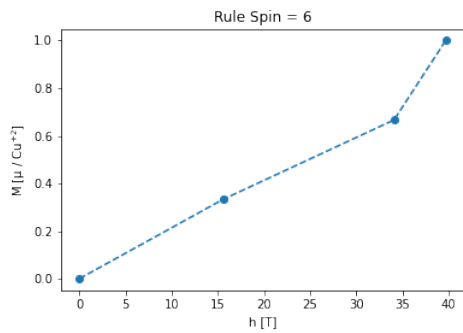
(a) Spin = 6 Magnezation

(b) Spin = 12 Magnezation
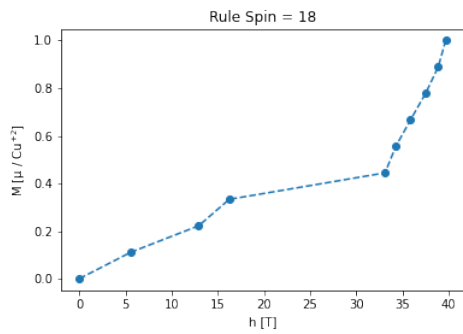
(c) Spin = 18 Magnezation
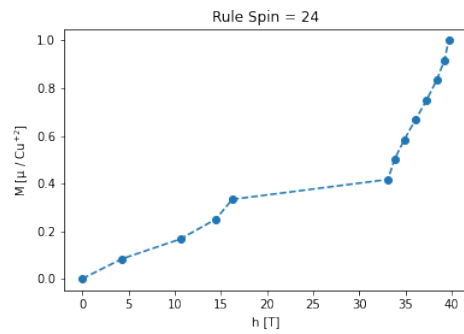
(d) Spin = 24 Magnezation
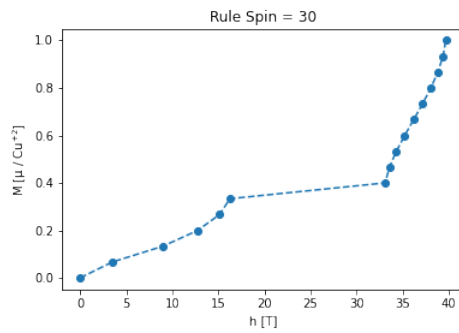
(e) Spin = 30 Magnezation

Figure 17: Magnetization plots by the model of Rule.

(a) Spin = 6 Excitation spectrum

(b) Spin = 12 Excitation spectrum

(c) Spin = 18 Excitation spectrum

(d) Spin = 24 Excitation spectrum

(e) Spin = 30 Excitation spectrum
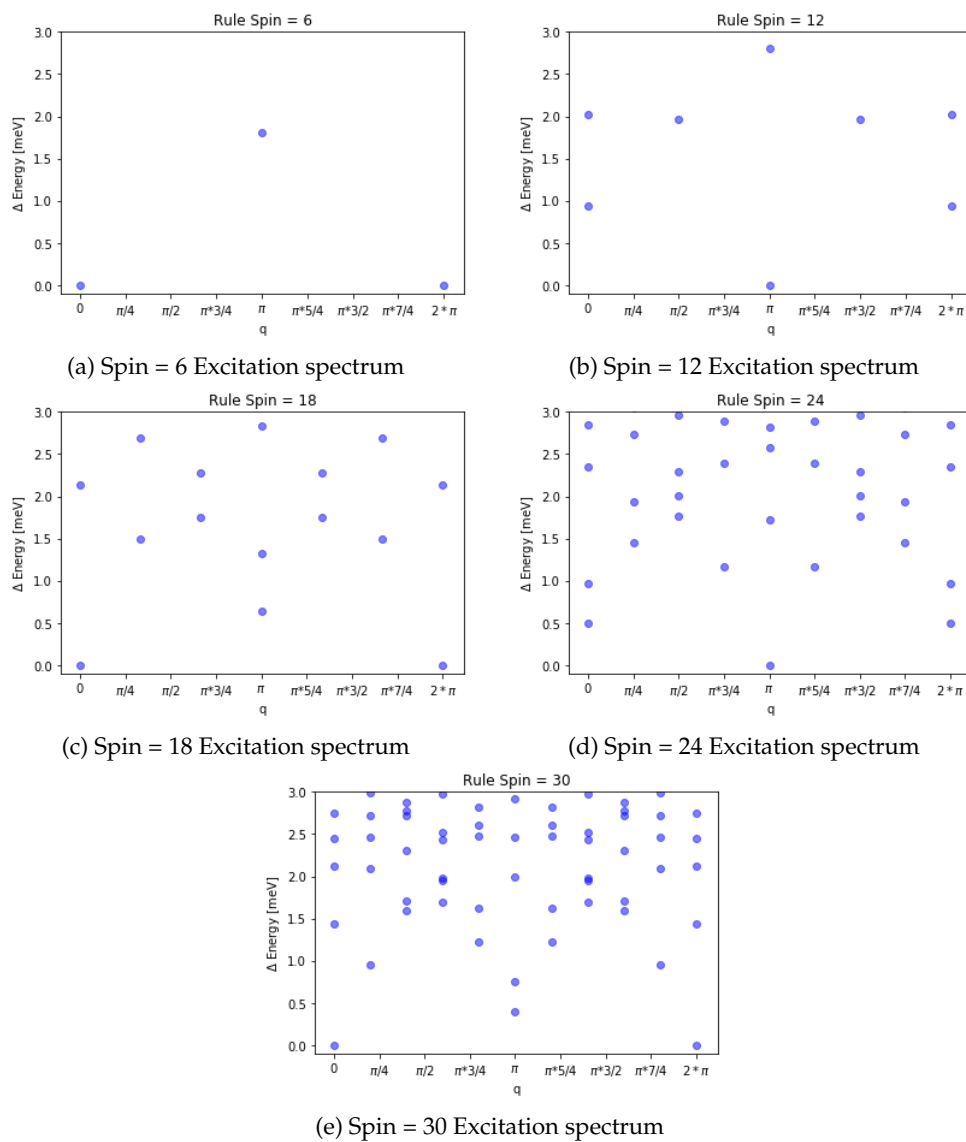
Figure 18: Excitation plots by the model of Rule.

All results can be found in Appendix A.

7.2 Magnetization

In this section, I will present the results obtained with RLexact for the magnetization in a given field for spin systems of sizes 24 and 30. For the magnetization plots I have taken the lowest energy for each magnetization, found the difference in energy for each of these and divided with the difference of magnetization. The y-axes of the magnetization plots are divided with the total magnetization to be able to enable comparison with the different system sizes and to compare with the results from the articles. Since RLexact gives energies in the different magnetization and does not calculate the Zeeman energy then this must be the energy difference between the magnetization. This can be shown:

$$H = H_H - hM \tag{78}$$

$$E_{M,h} = E(M) - hM \tag{79}$$

$$\Delta E = E_{M,h} - E_{M+1,h} = 0 \tag{80}$$

$$0 = E(M) - E(M+1) - h \tag{81}$$

$$h = -g\mu_B B \tag{82}$$

$$B = \frac{E(M+1) - E(M)}{g\mu_B} \tag{83}$$

Let us first look at the results of the exchange constants of those from Rule, seen in figure 19, first and start at the low magnetization. From 0T to around 12T the magnetization is almost a straight line and from 12T to around 17T it is growing fast. From 17T to 34T on 24 and 30 spin systems is where the $\frac{1}{3}$ magnetization plateau is observed, where after it goes up in a weak S-shape.

From Rule the next will be the data from the exchange constants by Kikuchi, which are shown in figure 20 and the experimental data (c) in the same figure. For both the 24 spin system and the 30 spin system from 0T to the beginning of the $\frac{1}{3}$ plateau the data is not a straight line, and has a weak S-shape just like Rule. The plateau starts at 14T and ends at 25T whereafter it increases slowly until 31T where it increases fast.

Lastly the data calculated with the exchange constants of Jeschke is in figure 21 with the plot from the article in the same figure as well. This has the same start as the two figures before with a weak S-shape but here it is shorter since the plateau starts at 10T and ends at 34T. After 34T the curve increases rapidly.

The calculated data from Jeschke does have a straight line from 0T to 9T with a sharp

kink from 9T to 10T where the plateau starts. It ends at 31T and increases rapidly afterwards.

(a) Rule Spin = 24 Magnezation   (b) Rule Spin = 30 Magnezation
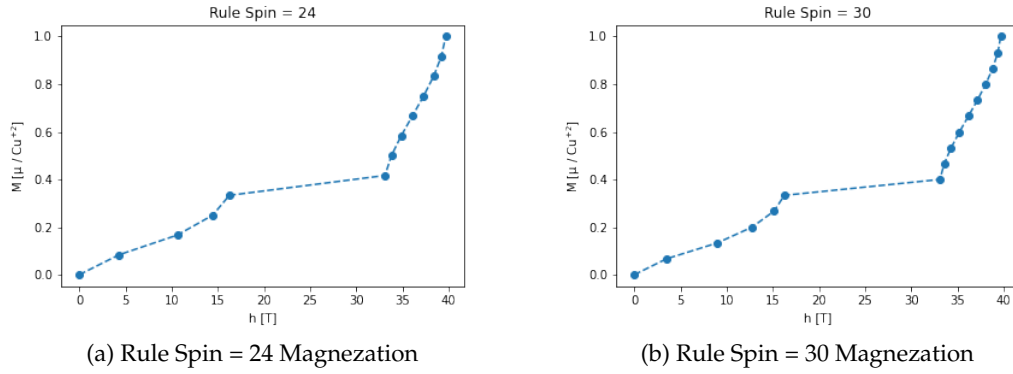
Figure 19: Magnetization plots by the model of Rule.
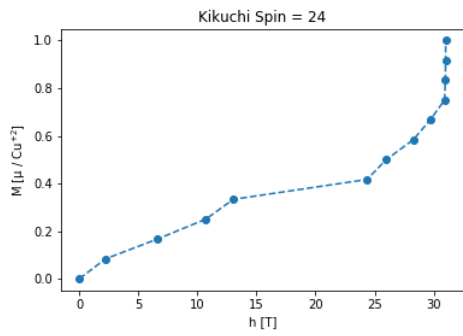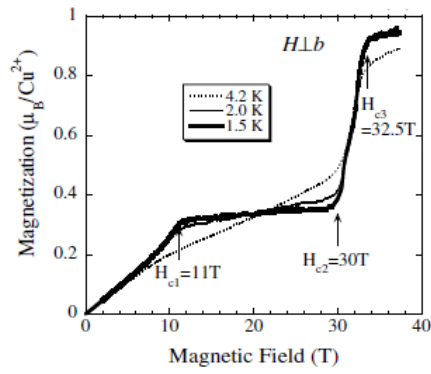
(a) Kikuchi Spin = 24 Magnezation
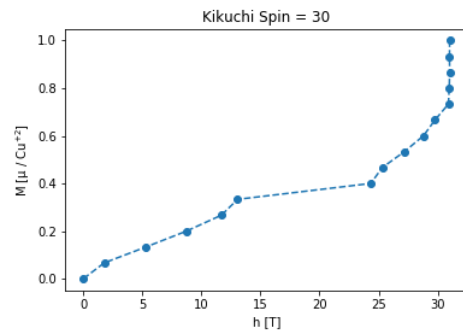
(b) Kikuchi Spin = 30 Magnezation

(c) Experimental data by Kikuchi

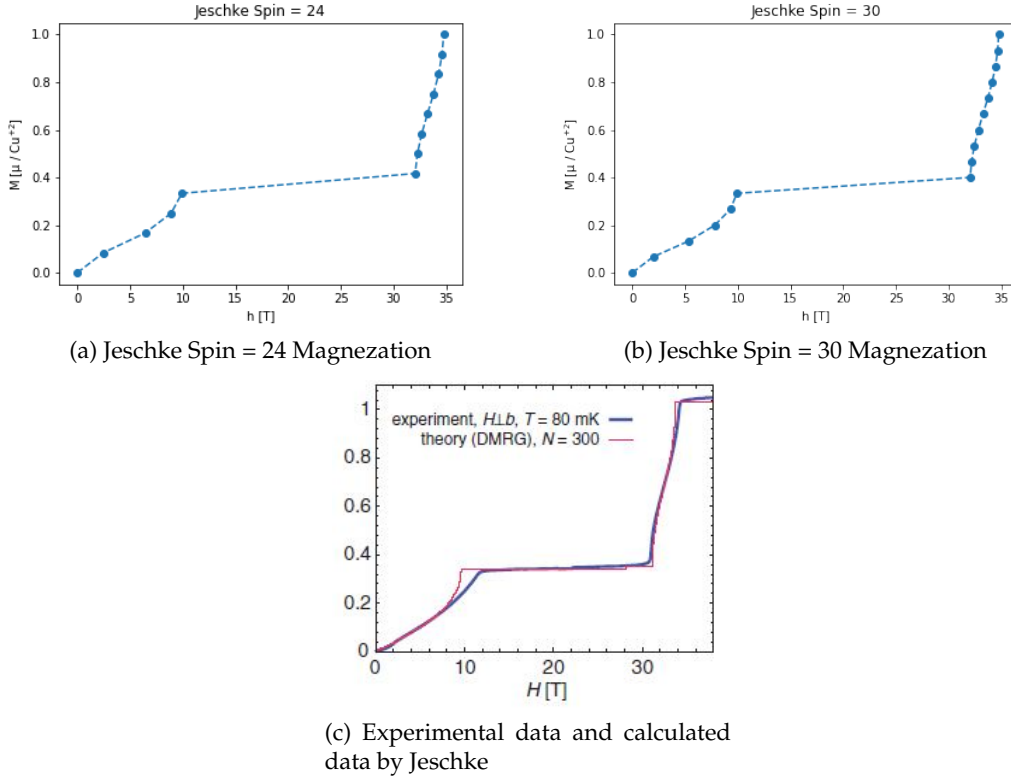Figure 20: Magnetization plots by the model of Kikuchi and experimental data from Kikuchi [11].

(a) Jeschke Spin = 24 Magnezation

(b) Jeschke Spin = 30 Magnezation

(c) Experimental data and calculated data by Jeschke

Figure 21: Magnetization plots by the model of Jeschke and experimental data from Jeschke [7].

7.3 Excitation

In this section, we will present the results obtained with RLexact for the excitation spectra of the different systems sizes, 18, 24 and 30. To do so, we have represented the Heisenberg energy as a function of the momentum, which in the first Brillouin zone is bounded by $q \in [0, 2\pi]$.

For Rule the excitation spectrum for the three different spin systems is not very occupied at the lower energies, as it is seen in figure 22 (c-e). To start let us look at the 30 spin system and the first mode that comes to eye is at (0,0) to (π,2.5) to (2π,0). There is another mode at (0,1.4) to (3/5π,1.6) to (π,1.4). There is something around (0,2.1) to (π,2.5) to (2π,2.1) but it is not visible in the 18 or 24 spin system. The last mentioned mode can be hard to determine since the density of the excitation are high in this region. In figure 23 we see the excitation spectrum calculated with the exchange constants from

Kikuchi [11] seen in table 2. It seems to have two modes. The first that came to mind was from (0,0 meV) to (π,1.5 meV) and down to (2 π, 0 meV) and the second from (0,0.8meV) to (2/5 π, 1.3) to (π,0.2meV). Energies above 1.5 meV are not really interesting but have been kept to be consistent in the plots.

The excitation spectrum in figure 24 with exchange constants from Jeschke [7] are seen in table 2. It seems to have a mode going from (0,0) to (π,1.1) to (2 π, 0) and another mode from (0,0) to (3/5 π, 1.0) to (π, 0.2). It also looks like there is something like a gap between the lower excitation and higher excitation, is around (0,1.1) to (4/5 π, 1.4) to (6/5 π, 1.4) to (2 π, 1.1), which is easier to see in the 18 spin plot where it is from (0,1.3) to (π,2.0) to (2π,1.3). Energies above 1.5 are not interesting here, but have been kept for consistent plots. The group of Jeschke have also performed excitation measurements with a field, but I will not cove these.

(a) Rule Spin = 18 Excitation

(b) Rule Spin = 24 Excitation

(c) Rule Spin = 30 Excitation

(d) Experimental data from Rule [21]
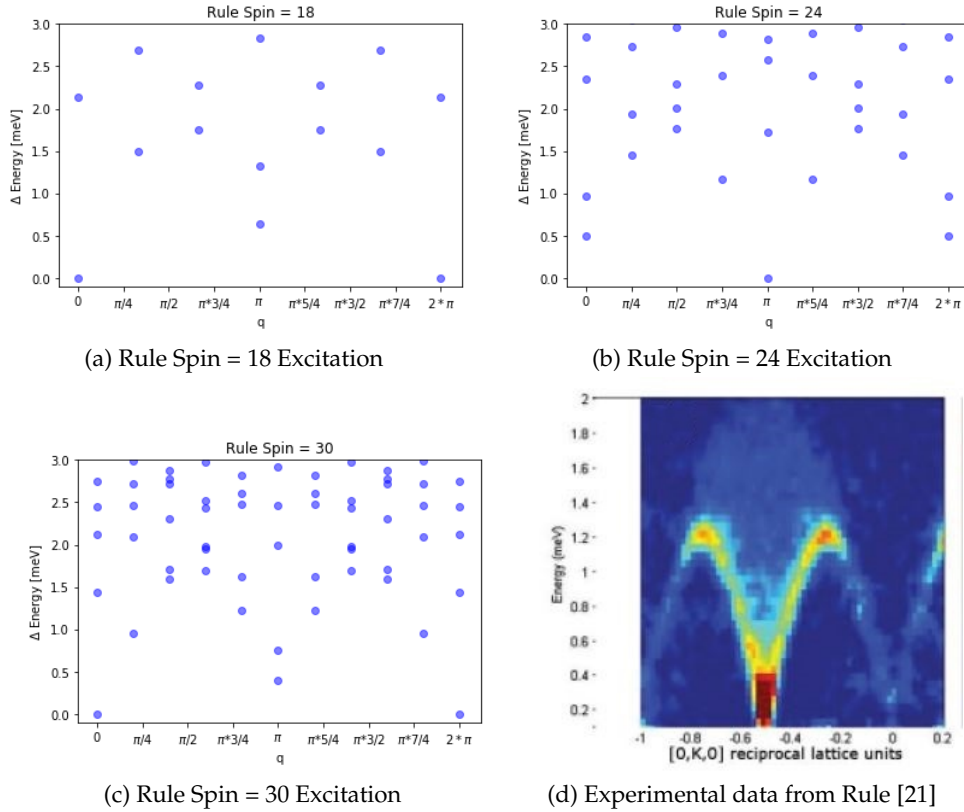
Figure 22: Excitation data of spin system with the model of Rule and experimental data provided by Rule.

54

(a) Kikuchi Spin = 18 Excitation

(b) Kikuchi Spin = 24 Excitation

(c) Kikuchi Spin = 30 Excitation
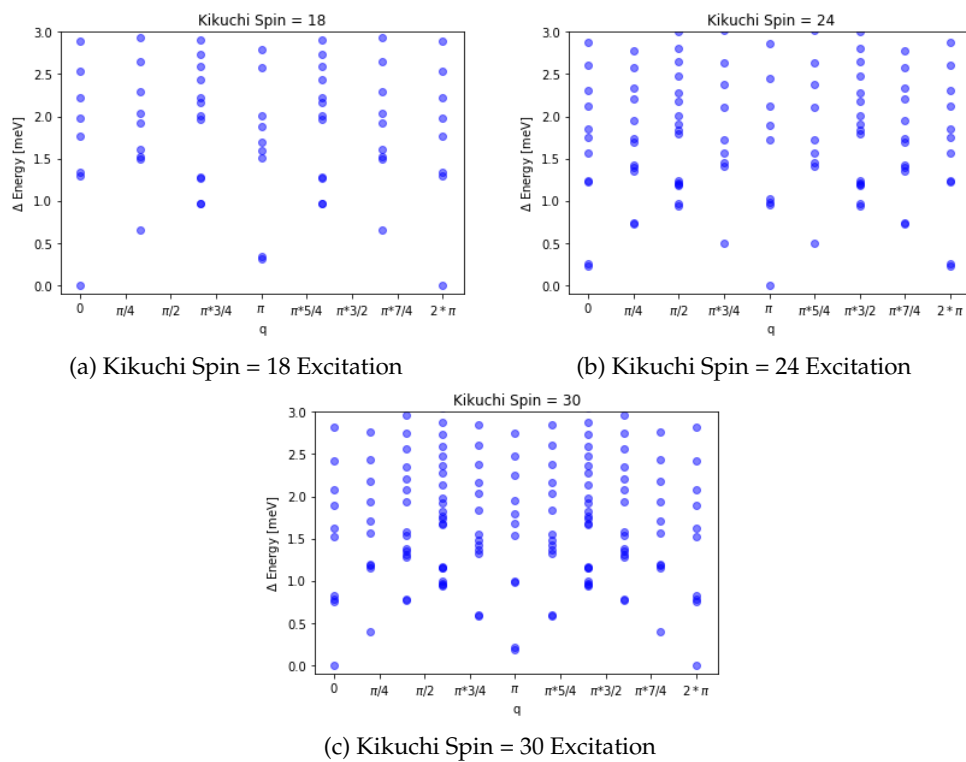
Figure 23: Excitation data of spin system with the model of Kikuchi.

(a) Jeschke Spin = 18 Excitation

(b) Jeschke Spin = 24 Excitation

(c) Jeschke Spin = 30 Excitation
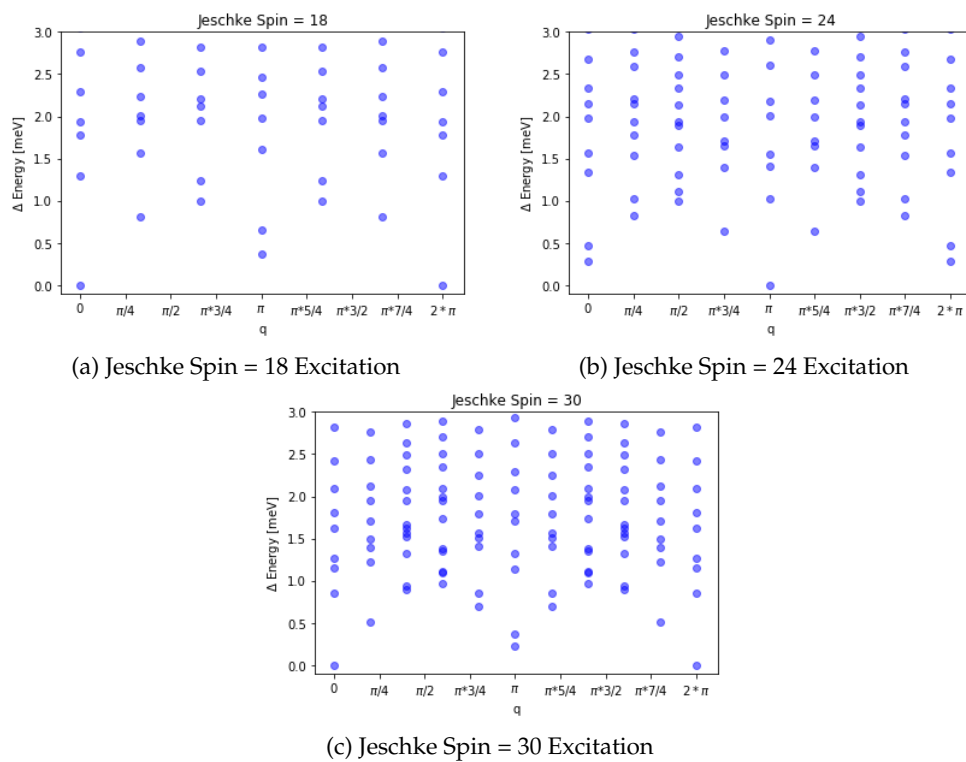
Figure 24: Excitation data of spin system with the model of Jeschke.

8 Discussion

The group of Kang has not been calculated in RLexact due to the fact that the model they have come up with has an exchange constant between the different diamond chains, which is not possible to do in RLexact (yet).

8.1 Magnetization comparison

Materials with $\frac{1}{3}$ magnetization and being able to find a fitting model for them are still an interesting and active field. This is where calculations by hand are hard and need some help from computational methods where Exact diagonalization, and hereunder RLexact is handy. The articles of Jeschke [7] and Kikuchi [11] both have excellent M(h) data to compare the calculations of RLexact with; and these are shown in figure figure 20 and 21. The Kikuchi plot of 1.5 K data and the experimental data of Jeschke agree on where the plateau starts (11T) and disagree lightly on where it stops (30T for Kikuchi and 31T for Jeschke). After the plateau there is a sharp rise in a weak s-shape in a couple of tesla (2-3T) until full M is reached.

To make a comparison of the data computed with RLexact with the plots from the articles let us start by talking about how the different calculations look in comparison with the experimental data. Since the articles use different values for the exchange constants the plateau is different for each of the articles. For Rule it seems to have moved the full plateau around 5T further up than the experimental data suggest. Rule has less of a straight line in comparison with the experimental data and the same goes for the end rise, which is not as steep as the experimental data suggest.

For Jeschke with a starting of the plateau at 10T and an end at 34T. The ending is as steep and looks very similar to the experimental data, but the beginning seems to have a little too much of a curve just before the plateau. The data from RLexact look even more similar to the theory data that Jeschke did with N=300. This enhances the credibility of our data.

The data calculated with RLexact with the model of Kikuchi is the one furthest away from the experimental data. The plateau starts from 14T and ending at 25T with a flat ending. It is also the model with the flattest and therefore most accurate start (from 0

to the start of the plateau).

8.2 Excitation comparison

Excitation spectra of materials contain important information and can be calculated by algorithms such as the Lanczos algorithm used in RLexact. Experimental data is provided by Rule [21]. The experimental data are from INS in an applied field of 14T. These can be found in figure 22 (d). The data of Rule has a mode going from $(-\pi,0)$ to $(\pi/2,2)$ to $(0,0)$ and another from $(-\pi,0)$ to $(-\pi\cdot3/4,1.4)$ to $(-\pi/2,0)$.

The three models give two groups, one where the spin wave mode is going to 1.0 meV and the other is where it goes to 1.5 meV. Rule is in the last group and is very close to the experimental data where the mode goes to 1.4 meV. The experimental data still have oscillations of $\pi/2$ where in the calculated data the oscillations go by π. The other mode in the experimental data by Rule go to 2.0 meV where the calculated data goes to 2.5 meV. These are the differences between the calculated data and the experimental data for Rules model and and some adjustments could be done to the model, for example with the Dzyaloshinskii-Moriya (DM) interaction as Rule writes about in [22]. This interaction is given by:

$$H_{DM} = \sum_{<i,j>} \mathbf{D}_{ij} \cdot (\mathbf{S}_i \times \mathbf{S}_j) \tag{84}$$

and is strongly influenced by the non centro symmetric J_1 and J_3 exchange interactions as seen in figure 25. Including the DM interaction in the model would change the model a little bit and could make the calculation of the model more accurate with the experimental data.
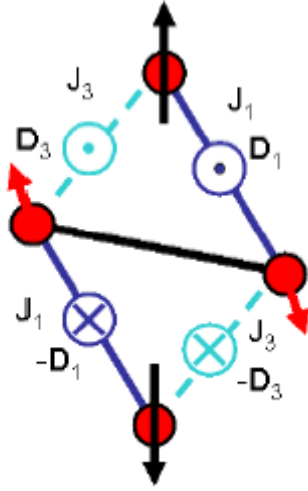
Figure 25: Dzyaloshinskii-Moriya (DM) interactions on the diamond shape units where the vertical direction corresponds to the b-axis. We define the notation of $\odot$ and $\otimes$ to represent antiparallel vectors since the actual orientation of the DM vector is not known[22].

The two other models (Kikuchi and Jeschke) look very similar, and the only difference in the spin wave mode is where the top of it is placed (3/5 π for Kikuchi and 2/5 π for Jeschke) and both have around the same energy difference at q = π. Another thing they have in common is that the top of the other mode is around 1.6 meV . This is a small difference in the excitation spectrum compared with the magnetization plots above and the exchange constants are not that different either, besides the fact that Jeschke has an exchange constant to couple the monomer spins. The top mode in the Jeschke excitation spectrum is not visible in my calculations and the oscillations are π in my calculations and 2π in Jeschke's data.

Since the diamond chain is calculated by RLexact as a 1D chain let us compare how a 1D nearest neighbor Heisenberg model would look, since these calculations since these calculations were done in RLexact as well. Can be seen in figure 26. The spin wave mode in this model goes from 0 meV to 1.5 meV with a oscillation of π. The other mode goes from 0 meV to 3 meV. The spin wave mode does look close to Rule's model. A difference is that Rules model the spin wave mode does not touch 0 meV at π but 2 π. This could be due to the finite size effect, which can be seen if we look at the trend of the 18, 24 and 30 spin systems.
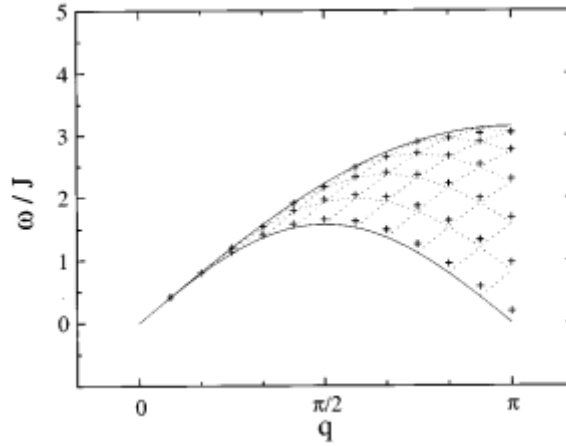
Figure 26: 1D NNM chain of N=24 in zero field, crosses are the spin wave continuum and dashed curves are dispersion for spin wave continuum states in the thermodynamical limit. [14]

8.3 RLexact

Some specific spin system sizes with specific (but unidentified) interactions have a problem where in a q in a high magnetization the ground state is not calculated correctly. The data can be seen in figure 27 and was easy to spot in the magnetization plots. This is not physically possible and has therefore been removed in the data for the results. This is done by opening the data files and removed some of the energies from the specific q in the magnetization which is acting up.

In some of the RLexact calculations there was a problem where some of the q's in different magnetizations stopped being calculated and restarted, this can be seen in figure 28. This means that the data was generated, but some of it was generated twice which is not useful. I think this could be due to some memory leak or maybe a problem with the cluster. I do not believe the error to be due to a problem in RLexact since it does not happen every time the calculations is done.

(a) Spin = 24 Magnezation

(b) Spin = 24 Magnezation

(c) Spin = 30 Magnezation
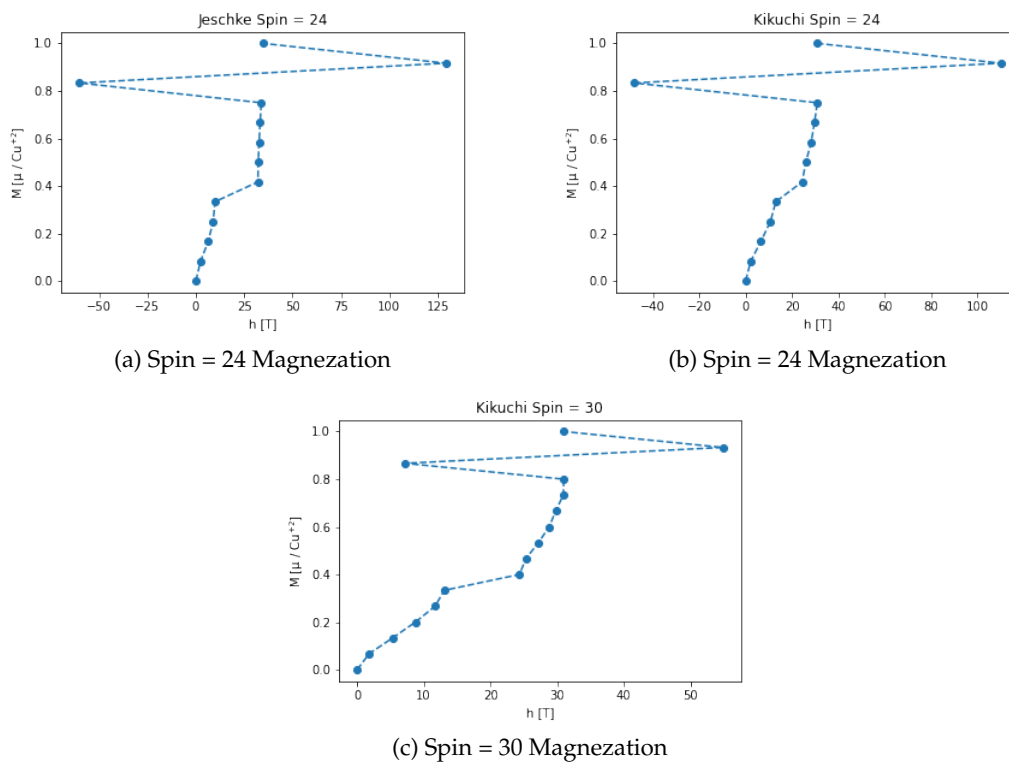
Figure 27: Magnetization energy calculation error.

Figure 28: Some kind of error on the cluster where RLexact was used, restart marked with red lines.

9 Conclusion

The work of this thesis can conclude that the exact diagonalization program RLexact is able to calculate and produce magnetization curves and excitation spectra for the model of azurite (1D diamond chain).

Comparisons between data calculated by RLexact and data from articles revealed the that the exchange constant from the study done by Rule best respresent the excitation spectrum, while the exchange constants from Jeschke best represent the magnetization curves.

10 Appendix
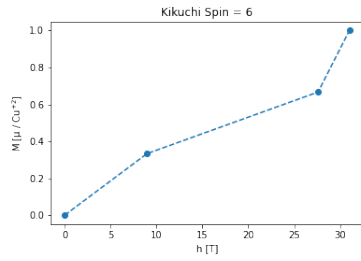
(a) Spin = 6 Magnetization
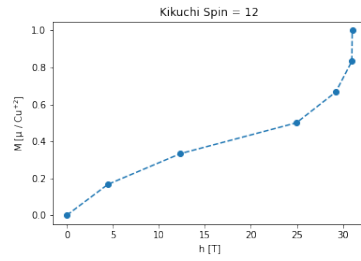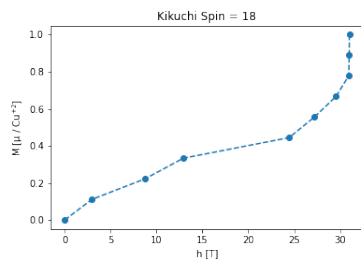
(b) Spin = 12 Magnetization

(c) Spin = 18 Magnetization
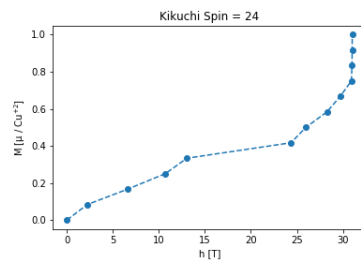
(d) Spin = 24 Magnetization
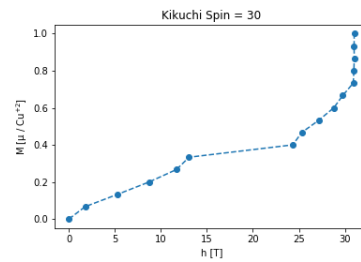
(e) Spin = 30 Magnetization
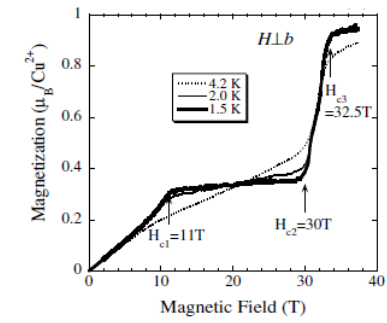
(f) Magnetization data from Kikuchi [11]

Figure 29: Magnetization data calculated by RLexact with exchange constants from Kikuchi and magnetization data from Kikuchi.
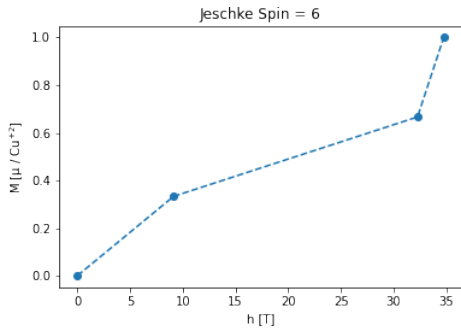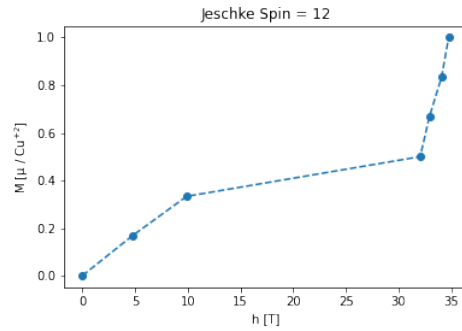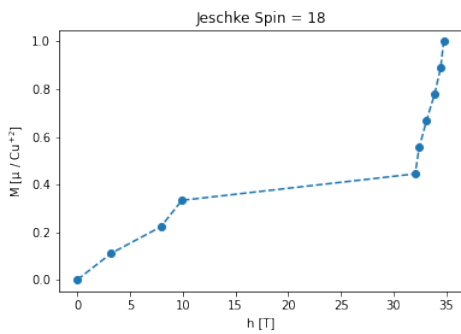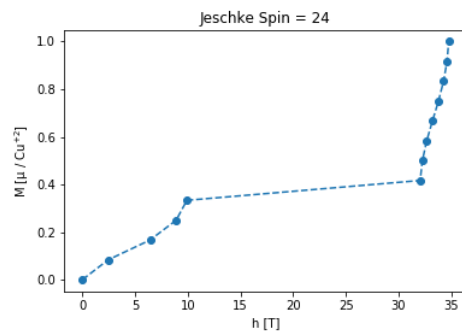
(a) Spin = 6 Excitation spectrum

(b) Spin = 12 Excitation spectrum

(c) Spin = 18 Excitation spectrum

(d) Spin = 24 Excitation spectrum

(e) Spin = 30 Excitation spectrum
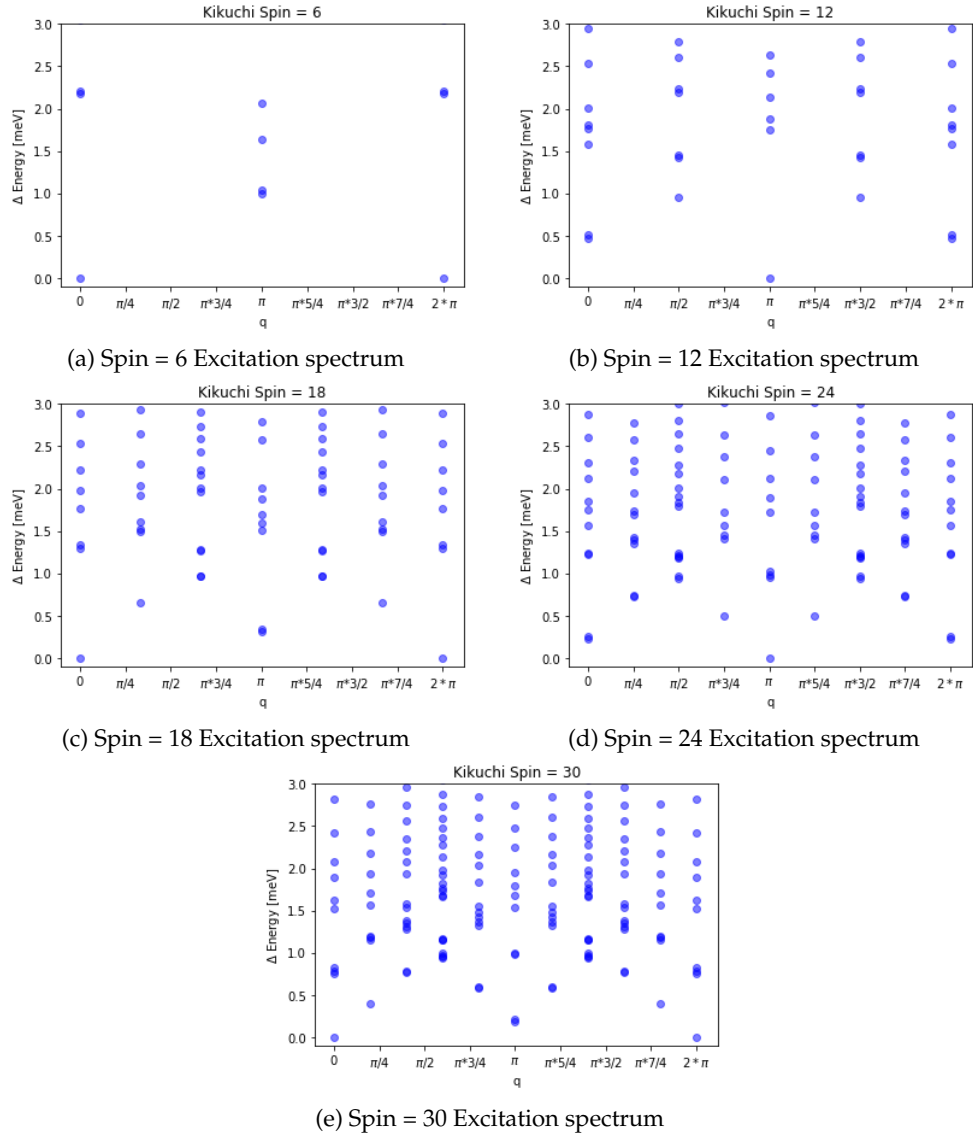
Figure 30: Excitation data calculated by RLexact with exchange constants from Kikuchi.
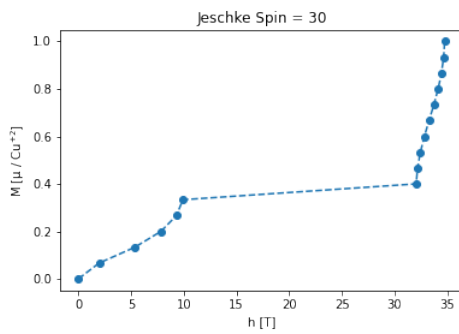
(a) Spin = 6 Magnetization

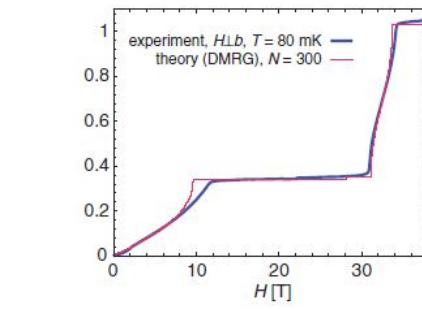
(b) Spin = 12 Magnetization

(c) Spin = 18 Magnetization

(d) Spin = 24 Magnetization

(e) Spin = 30 Magnetization

(f) Magnetization data from Jeschke [7]

Figure 31: Magnetization data calculated by RLexact with exchange constants from Jeschke and magnetization data from Jeschke.
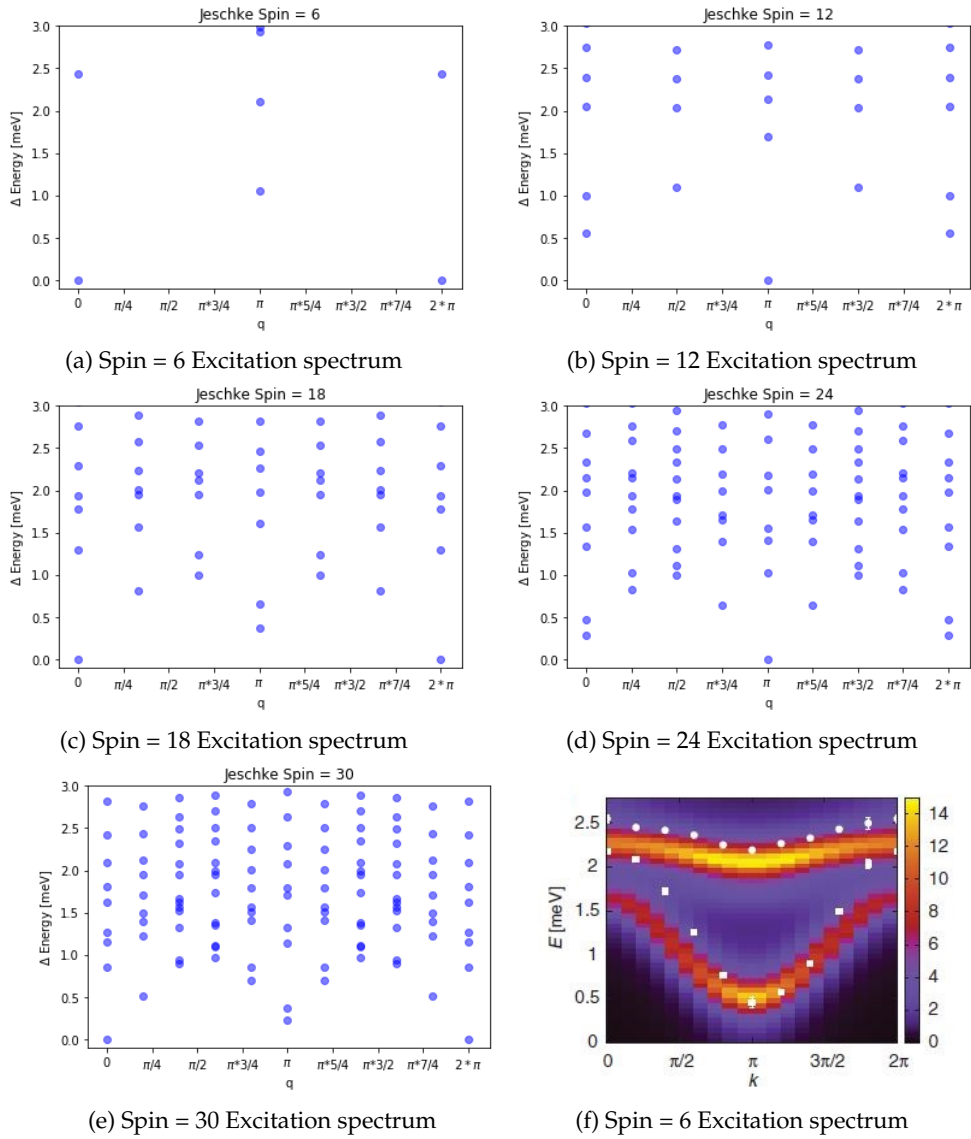
(a) Spin = 6 Excitation spectrum

(b) Spin = 12 Excitation spectrum

(c) Spin = 18 Excitation spectrum

(d) Spin = 24 Excitation spectrum

(e) Spin = 30 Excitation spectrum

(f) Spin = 6 Excitation spectrum

Figure 32: Excitation data calculated by RLexact with exchange constants from Jeschke and Excitation data from Jeschke.

References

[1] Stephen Blundell. *Magnetism in condensed matter*. Oxford master series in condensed matter physics. Oxford University Press, 1 edition, 2001.

[2] J.S Caux. Correlation functions of integrable models: A description of the abacus algorithm. *Journal of mathematical physics*, 50(9):095214–095214–18, 2009.

[3] A. W Garrett, S. E Nagler, D. A Tennant, B. C Sales, and T Barnes. Magnetic excitations in the s=1/2 alternating chain compound $(vo)_2 p_2 o_7$. 1997.

[4] A Honecker and A Läuchli. Frustrated trimer chain model andcu3cl6(h2o)22h8c4so2in a magnetic field. *Physical review. B, Condensed matter*, 63(17):174407, 2001.

[5] Sofie Janas. The quantum phase transition in transverse field ising and ising-like anistropic systems: a numerical study, 2017.

[6] Sofie Janas. Neutron spectroscopy studies of geometrically frustrated antiferromagnets, 2020.

[7] Harald Jeschke, Ingo Opahle, Hem Kandpal, Roser Valentí, Hena Das, Tanusri Saha-Dasgupta, Oleg Janson, Helge Rosner, Andreas Brühl, Bernd Wolf, Michael Lang, Johannes Richter, Shijie Hu, Xiaoqun Wang, Robert Peters, Thomas Pruschke, and Andreas Honecker. Multistep approach to microscopic models for frustrated quantum magnets: the case of the natural mineral azurite. *Physical review letters*, 106(21):217201–217201, 2011.

[8] Claire Lhuillier John T. Chalker and Grégoire Misguich et al. *Introduction to Frustrated Magnetism Materials, Experiments, Theory*. Springer Series in Solid-State Sciences, 164. Springer Berlin Heidelberg, Berlin, Heidelberg, 1st ed. 2011. edition, 2011.

[9] J Kang, C Lee, R K Kremer, and M-H Whangbo. Consequences of the intrachain dimer–monomer spin frustration and the interchain dimer–monomer spin exchange in the diamond-chain compound azurite cu3(co3)2(oh)2. *Journal of physics. Condensed matter*, 21(39):392201–, 2009.

[10] H KIKUCHI, Y FUJII, M CHIBA, S MITSUDO, T IDEHARA, T TONEGAWA, K OKAMOTO, T SAKAI, T KUWAI, and H OHTA. Experimental observation of the 1/3 magnetization plateau in the diamond-chain compound cu3(co3)2(oh)2. *Physical review letters*, 94(22):227201.1–227201.4, 2005.

[11] Hikomitsu Kikuchi, Yutaka Fujii, Meiro Chiba, Seitaro Mitsudo, Toshitaka Idehara, Takashi Tonegawa, Kiyomi Okamoto, Tôru Sakai, Tomohiko Kuwai, Koichi Kindo, Akira Matsuo, Wataru Higemoto, Kusuo Nishiyama, Mladen Horvatić, and Claude Bertheir. Magnetic properties of the diamond chain compound cu3(co3)2(oh)2. *Progress of theoretical physics. Supplement*, 159(159):1–10, 2005.

[12] Hyun-Joo Koo and Myung-Hwan Whangbo. Analysis of the spin lattice model for the spin-gapped layered compounds na(3)cu(2)sbo(6) and na(2)cu(2)teo(6) on the basis of electronic structure calculations. *Inorganic chemistry*, 47(1):128–133, 2008.

[13] K. Lefmann. Manual for the exact diagonalization package rlexact version 3.1, 2016.

[14] K Lefmann and C Rischel. Dynamical correlation functions of the s=1/2 nearest-neighbor and haldane-shastry heisenberg antiferromagnetic chains in zero and applied fields. *Physical review. B, Condensed matter*, 54(9):6340–6350, 1996.

[15] Kim Lefmann. *Neutron Scattering: Theory, Instrumentation and Simulation*. 2020.

[16] H.-J Mikeska and C Luckmann. Dynamics of a distorted diamond chain. *Physical review. B, Condensed matter and materials physics*, 77(5):054405, 2008.

[17] Yoko MIURA, Riu HIRAI, Yoshiaki KOBAYASHI, and Masatoshi SATO. Spin-gap behavior of na3cu2sbo6 with distorted honeycomb structure. *Journal of the Physical Society of Japan*, 75(8):84707–, 2006.

[18] Yoshiyuki Nishio. Pigments used in japanese paintings. *The Paper Conservator*, 11(1):39–45, 1987.

[19] John P Perdew, Kieron Burke, and Matthias Ernzerhof. Generalized gradient approximation made simple [phys. rev. lett. 77, 3865 (1996)]. *Physical review letters*, 78(7):1396–1396, 1997.

[20] W.H. Press. *Numerical recipes in C : the art of scientific computing ; W. H. Press..[et al.].* Cambridge University Press, Cambridge, 2nd. ed. edition, 1996.

[21] K. Rule, A. Wolter, S. Süllow, D. Tennant, A. Brühl, S. Köhler, B. Wolf, M. Lang, and J. Schreuer. Nature of the spin dynamics and 1/3 magnetization plateau in azurite. *Physical review letters*, 100 11:117202, 2008.

[22] K. C. Rule, M. Reehuis, M. C. R. Gibson, B. Ouladdiaf, M. J. Gutmann, J.-U. Hoffmann, S. Gerischer, D. A. Tennant, S. Süllow, and M. Lang. Magnetic and crystal structure of azurite $cu_3(co_3)_2(oh)_2$ as determined by neutron diffraction. *Phys. Rev. B*, 83:104401, Mar 2011.

[23] K. C Rule, D. A Tennant, J.-S Caux, M. C. R Gibson, M. T. F Telling, S Gerischer, S Süllow, and M Lang. Dynamics of azurite cu3(co3)2(oh)2in a magnetic field as determined by neutron scattering. *Physical review. B, Condensed matter and materials physics*, 84(18):184419, 2011.

[24] Anders W Sandvik. Computational studies of quantum spin systems. 2011.

[25] T Tonegawa, K Okamoto, T Hikihara, Y Takahashi, and M Kaburagi. Ground state of an s=1/2 distorted diamond chain in a finite magnetic field. *The Journal of physics and chemistry of solids*, 62(1):125–128, 2001.

[26] Dr. Martijn Marsman Dr. Merzuk Kaltak Dr. Ferenc Karsai Dr. Martin Schlipf Univ. Prof. Dr. Georg Kresse, Dr. Doris Vogtenhuber. Vienna ab initio simulation. `https://www.vasp.at/`. Accessed: 2021-10-29.